

Photonic and EO Device Characterization

M. An
M. Callahan
J. Kierstad
R. Lancto
P. Tedrow
W. Waters

Solid State Scientific Corporation
27-2 Wright Rd
Hollis, NH

July 2000

Final Report

Approved for Public Release; Distribution Unlimited



AIR FORCE RESEARCH LABORATORY
Sensors Directorate
80 Scott Dr
AIR FORCE MATERIEL COMMAND
Hanscom AFB, MA 01731-2909

DTIC QUALITY INSPECTED 4

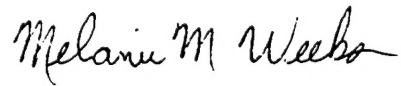
20000911 126

Title of Report: Photonic & EO Device Characterization

PUBLICATION REVIEW

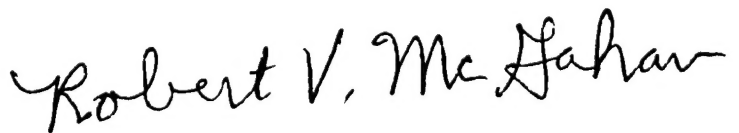
This report has been reviewed and is approved for publication.

APPROVED:



Melanie M. Weeks, Project Engineer
IR Sensor Technology Branch
Electromagnetics Technology Division

FOR THE DIRECTOR



Dr. Robert V. McGahan, Technical Advisor
Electromagnetics Technology Division

REPORT DOCUMENTATION PAGE			Form Approved OMB No. 0704-0188	
Public reporting burden for this collection of information is estimated to average 1 hour per response, including the time for reviewing instructions, searching existing data sources, gathering and maintaining the data needed, and completing and reviewing the collection of information. Send comments regarding this burden estimate or any other aspect of this collection of information, including suggestions for reducing this burden, to Washington Headquarters Services, Directorate for Information Operations and Reports, 1215 Jefferson Davis Highway, Suite 1204, Arlington, VA 22202-4302, and to the Office of Management and Budget, Paperwork Reduction Project (0704-0188), Washington, DC 20503.				
1. AGENCY USE ONLY (Leave blank)		2. REPORT DATE 2000		3. REPORT TYPE AND DATES COVERED Final 6 June 95 - 6 June 99
4. TITLE AND SUBTITLE Photonic & EO Device Characterization			5. FUNDING NUMBERS F19628-95-C-0083 PEC: 62702F, 61102F PR: 4600, 2305 TA: 17, 18, 19, C1 WU: 997013	
6. AUTHOR(S) An, M.; Callahan, M.; Kierstead, J.; Lancto, R.; Tedrow, P.; Waters, W.				
7. PERFORMING ORGANIZATION NAME(S) AND ADDRESS(ES) Solid State Scientific Corporation 27-2 Wright Road Hollis, NH 03049			8. PERFORMING ORGANIZATION REPORT NUMBER	
9. SPONSORING/MONITORING AGENCY NAME(S) AND ADDRESS(ES) AFRL/SNHI 80 Scott Road Hanscom AFB, MA 01731-2909			10. SPONSORING/MONITORING AGENCY REPORT NUMBER AFRL-SN-HS-TR-2000-002	
11. SUPPLEMENTARY NOTES				
12a. DISTRIBUTION AVAILABILITY STATEMENT Approved for public release Distribution unlimited			12b. DISTRIBUTION CODE	
13. ABSTRACT (Maximum 200 words) This report represents the work of eight (8) researchers providing support for six (6) ongoing programs at AFRL/SNH. The research topics include: (i) Optical properties of turbulent media. (ii) InP based HEMPTs, MISFETs, and MSMs. (iii) Bulk crystal growth of ZnO and GaN substrates. (iv) Bulk crystal growth of InP substrates. (v) Mathematics of chromotomography. (vi) Thermionic emission based thermal detectors. In order to establish the context of the work, this report is best read alongside the published papers and presentations of the primary AFRL scientists conducting the research. Among the new concepts and achievements that emerged from this work are: a new class of uncooled thermal infrared imagers based on Schottky diodes, two orders of magnitude improvement in the convergence rate of chromotomography algorithms, a new amenothermal growth technique for GaN substrates, and a 25 GHz. InP wafer thinned optical receiver.				
14. SUBJECT TERMS Silicides, infrared detector, electro-optic materials, indium phosphide, reconstruction algorithms, zinc oxide, nitrides			15. NUMBER OF PAGES 60	
			16. PRICE CODE	
17. SECURITY CLASSIFICATION OF REPORT UNCLASSIFIED	18. SECURITY CLASSIFICATION OF THIS PAGE UNCLASIFIED	19. SECURITY CLASSIFICATION OF ABSTRACT UNCLASSIFIED	20. LIMITATION OF ABSTRACT UL	

GENERAL INSTRUCTIONS FOR COMPLETING SF 298

The Report Documentation Page (RDP) is used in announcing and cataloging reports. It is important that this information be consistent with the rest of the report, particularly the cover and title page. Instructions for filling in each block of the form follow. It is important to **stay within the lines** to meet **optical scanning requirements**.

Block 1. Agency Use Only (Leave blank).

Block 2. Report Date. Full publication date including day, month, and year, if available (e.g. 1 Jan 88). Must cite at least the year.

Block 3. Type of Report and Dates Covered. State whether report is interim, final, etc. If applicable, enter inclusive report dates (e.g. 10 Jun 87 - 30 Jun 88).

Block 4. Title and Subtitle. A title is taken from the part of the report that provides the most meaningful and complete information. When a report is prepared in more than one volume, repeat the primary title, add volume number, and include subtitle for the specific volume. On classified documents enter the title classification in parentheses.

Block 5. Funding Numbers. To include contract and grant numbers; may include program element number(s), project number(s), task number(s), and work unit number(s). Use the following labels:

C - Contract	PR - Project
G - Grant	TA - Task
PE - Program Element	WU - Work Unit Accession No.

Block 6. Author(s). Name(s) of person(s) responsible for writing the report, performing the research, or credited with the content of the report. If editor or compiler, this should follow the name(s).

Block 7. Performing Organization Name(s) and Address(es). Self-explanatory.

Block 8. Performing Organization Report Number. Enter the unique alphanumeric report number(s) assigned by the organization performing the report.

Block 9. Sponsoring/Monitoring Agency Name(s) and Address(es). Self-explanatory.

Block 10. Sponsoring/Monitoring Agency Report Number. (If known)

Block 11. Supplementary Notes. Enter information not included elsewhere such as: Prepared in cooperation with....; Trans. of....; To be published in.... When a report is revised, include a statement whether the new report supersedes or supplements the older report.

Block 12a. Distribution/Availability Statement.

Denotes public availability or limitations. Cite any availability to the public. Enter additional limitations or special markings in all capitals (e.g. NOFORN, REL, ITAR).

DOD - See DoDD 5230.24, "Distribution Statements on Technical Documents."

DOE - See authorities.

NASA - See Handbook NHB 2200.2.

NTIS - Leave blank.

Block 12b. Distribution Code.

DOD - Leave blank.

DOE - Enter DOE distribution categories from the Standard Distribution for Unclassified Scientific and Technical Reports.

NASA - Leave blank.

NTIS - Leave blank.

Block 13. Abstract. Include a brief (*Maximum 200 words*) factual summary of the most significant information contained in the report.

Block 14. Subject Terms. Keywords or phrases identifying major subjects in the report.

Block 15. Number of Pages. Enter the total number of pages.

Block 16. Price Code. Enter appropriate price code (*NTIS only*).

Blocks 17. - 19. Security Classifications. Self-explanatory. Enter U.S. Security Classification in accordance with U.S. Security Regulations (i.e., UNCLASSIFIED). If form contains classified information, stamp classification on the top and bottom of the page.

Block 20. Limitation of Abstract. This block must be completed to assign a limitation to the abstract. Enter either UL (unlimited) or SAR (same as report). An entry in this block is necessary if the abstract is to be limited. If blank, the abstract is assumed to be unlimited.

Table of Contents

Table of Contents	2
John Kierstead	3
William Waters	15
Michael Callahan	28
Robert Lancto	41
Myoung An	46
Prabha Tedrow	59
Financials	61

TECHNICAL ACTIVITY:

The following report covers a 4 year period of research. This research covers a variety of topics which include the following: gas cells, noise, air turbulence diagnostics, radio frequency coil design for spectral holeburning, sample preparation for optical data storage experiments, supersonic beam component construction, and cryostat setup.

Gas Cells:

Gas cells are useful for the observation of optical-atomic interactions in a closed system. Data can be taken under varying conditions, e.g. pressure, temperature or optical power. The problem is to construct a vacuum-tight, non-magnetic cell in which a sodium atmosphere can be contained at elevated temperatures. The material chosen was copper. The main body of this cell (Fig.1) (10"long, 1 1/2"dia, 1/8"wall) and the observation arm (10"long, 1/2"dia, 1/16" wall) have to be joined together at six different places with a braze material that melts at approximately 700°C. Torch brazing in the atmosphere was not a choice because of the inherent oxide buildup. It was decided to vacuum braise in a bell-jar system using a Lepel induction generator as a heat source. Initial attempts were not very promising because the target temperature was not reached after 30 minutes of operation. Much effort was put into optimizing the coil that surrounds the work piece. Various changes to the diameter, length, and turn spacing resulted in a configuration that raised the work piece up to the desired temperature in less than 10 minutes.

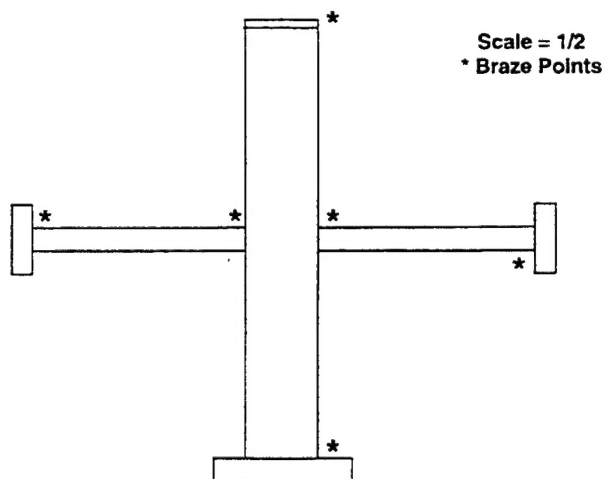


Figure 1. The main body of the vacuum-tight, non-magnetic gas cell.

Typical conventional braze materials have additives of either cadmium or zinc. Both of these materials are unsuitable for operation in a high vacuum system because of their high vapor pressures at elevated temperature. There are brazes available that do not have these additives. The one chosen was manufactured by Lucas Milhaupt, Braze 603 (60% Ag, 30%Cu, 10%Sn). Although these materials solve the vacuum problem, they have a wetting problem of their own. Most of the difficulty occurred joining the two tubes together. When the braze ring placed at the junction of the two tubes was brought up to temperature, a large portion of the braze material rolled off of the copper. A unique solution was used (Fig.2), which involved wrapping 7 or 8

turns of copper wire, #26 gauge around the 1/2" diameter arms. This provided a wetting reservoir to hold the braze material while the surrounding material came up to temperature and the brazing material flowed to make a successful joint.

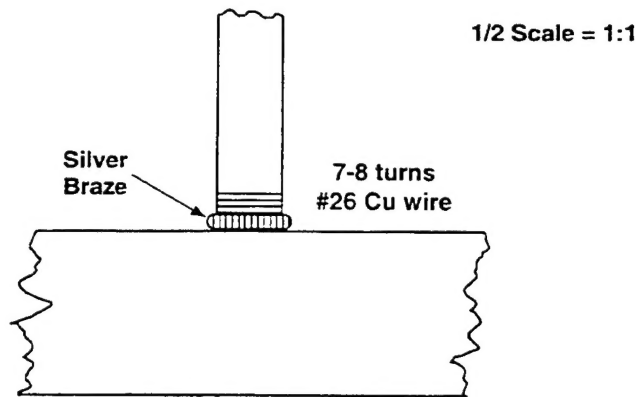


Figure 2. The new technique of wrapping copper wire around the arms to hold the braze in place.

Noise:

Noise, its behavior and reduction is of considerable experimental interest. Noise generated in laser based experiments is dual in nature, consisting of both electronic and optical noise. Electronic noise generally considered as Johnson, photocurrent and amplifier input noise. Optical noise generated in a laser has a $1/f$ component as well as shot noise. Marginal experiments are made possible by the improvement of signal to noise ratio, i.e. the reduction of noise from any contributing sources. The cancellation of $1/f$ noise produced by the laser is possible by subtracting the split laser beams in a pair of differentially configured photodiodes (Fig.3). The signal amplifier chosen was a Comlinear, CLC425. This is a low noise, wide bandwidth (1.2GHz) op-amp.

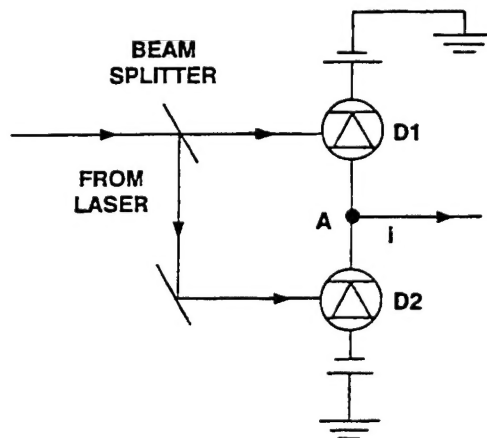


Figure 3. Illustrates the setup designed to cancel the $1/f$ noise produced by the laser.

The first construction attempts at using this op-amp with conventional point to point wiring turned out to be impossible. Oscillations continued in spite of the revised layout, components and bypassing. The problem required a more hygienic solution. It was discovered

that there was a printed circuit board available that Comlinear had designed for the CLC425. The amplifier was reconstructed on one of these boards. The photodiodes were placed in close proximity in order to reduce stray capacitance and lead inductance. This circuit board version of the amplifier proved to be free of all spurious oscillations.

Experimental results using a differential diode photodetector as a means of reducing laser noise resulted in an overall noise reduction of 10 to 15db. It was intended to use this subtraction method for the total noise reduction. Unfortunately this was not adequate and additional amplitude fluctuation reduction will have to be done on the two dye laser beams. Work is currently being done on an amplitude stabilization scheme utilizing an electro-optic modulator. This device whose index of refraction is voltage sensitive can be used as a means of converting the amplitude fluctuations of the light to a voltage which can be used as a control signal in a feedback stabilization system (Fig.4). Two stabilization systems will be needed and both beams will be independently, amplitude stabilized before the final differential diode subtraction. One stabilizer has been constructed and noise measurements were successful.

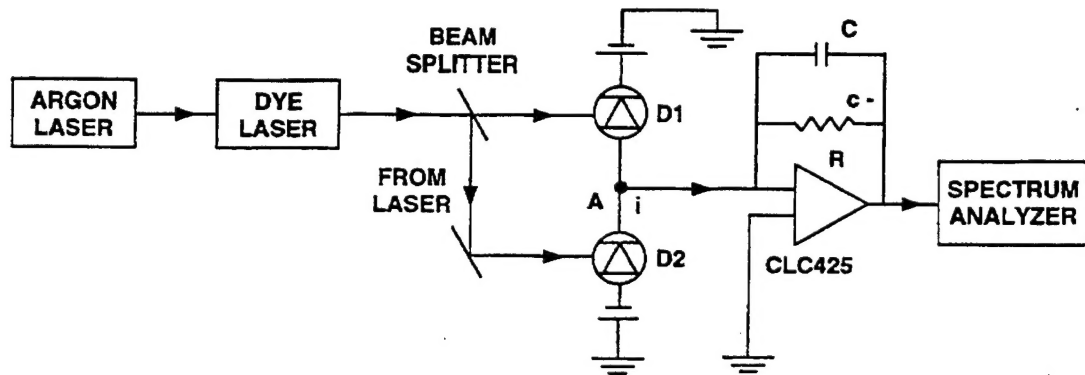


Figure 4. The design of the new feedback stabilization system.

Air Turbulence Diagnostics:

Diagnosis of turbulent flowing air is of considerable interest in a variety of fields. Diagnostic techniques already exist for the analysis of lower velocity air streams. An investigation of the possibility of detecting the interaction of a laser beam with the rapidly varying flow produced at the output of a nozzle in a vacuum chamber is being conducted. The basic idea consists of bleeding air through a nozzle into a chamber evacuated by a high capacity mechanical pump. This chamber (a six-way cross) has two windows which allow the laser beam to pass through, probing the turbulent region. The output beam deflection is detected using a pinhole and a high-speed photodetector and displayed on an oscilloscope.

A suitable nozzle of the desired geometry was not available for this experiment, so one had to be fabricated. The final solution was to insert a piece of thin shim stock into a piece of thin wall stainless steel tubing (1/8" o.d.) and clamp down on the tubing between two parallel jaws. This technique produced nozzles with an output aperture of approximately 0.005" x 0.250". Preliminary measurements have been made at atmospheric pressure and turbulence "noise" has been observed.

The goal was to construct rubidium seeded flow chambers. It was necessary to use rubidium, instead of sodium, because the larger hyperfine splitting in rubidium allows the ground

state to be resolved in the presence of Doppler broadening. This is important because the first step in the planned Raman NMR imaging scheme is to optically pump the atoms into a single hyperfine ground state.

Two flow chambers have been constructed. One consists of a rubidium seeded buffer gas chamber with interchangeable nozzles. One nozzle is designed for supersonic flow and its purpose is to provide a well characterized flow pattern to test the Raman NMR concept (Fig.5). The second nozzle is similar to the one described above, and is capable of generating turbulent flow with variations on the time scale of 10's of microseconds.

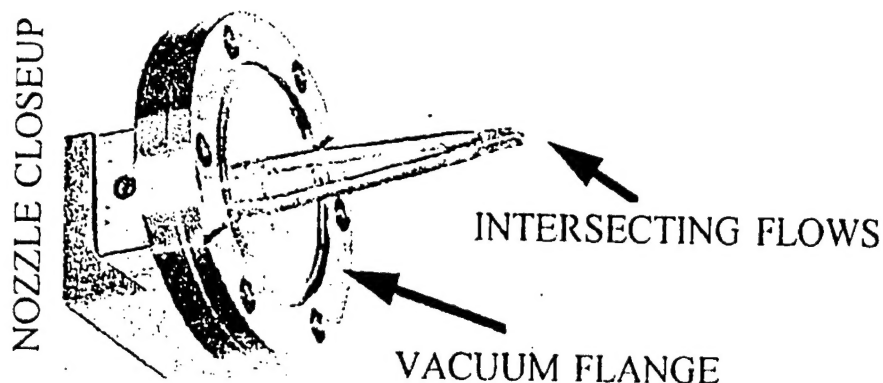


Figure 5. The supersonic flow nozzle.

The second flow chamber consists of two nozzles of the type described above, arranged so that the emitted jets collide at an angle of about 10 degrees. Each nozzle has a separate gas and rubidium source. This allows the use of different buffer gasses, for example helium and argon in each nozzle, and also gives the option of seeding each jet independently (Fig.6).

Radio Frequency Coil Design For Spectral Holeburning:

The goal of the Raman excited spin echo experiment is to develop an optical image cache memory that can capture 1000's of consecutive frames of information at microsecond frame rates. This would open the way for a detailed analysis of high-speed turbulent flows and direct comparison with theory. The plan is to use spectral holeburning materials consisting of rare earth ions, such as Europium (Eu) and Praseodymium (Pr), doped in a crystal host.

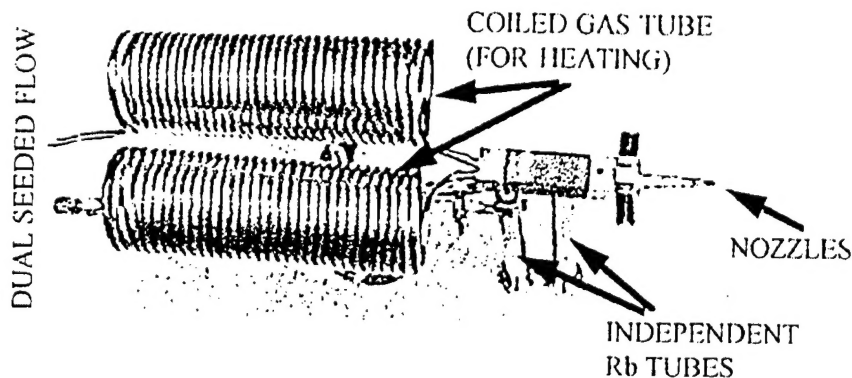


Figure 6. The second flow chamber's two nozzles.

Progress so far consists of the construction of an experimental setup for spectral holeburning using rare earth doped crystals and preliminary, continuous wave measurements of the properties of spin coherence. Both Eu and Pr doped crystals of Y_2SiO_5 have been studied. The first experiment is to study the Raman heterodyne signals in these materials. These signals have been seen in Pr; however, the signal has some interesting features as yet unexplained.

In order to observe the nuclear resonance in these rare earth ions, it is necessary to produce an external magnetic field perpendicular to the crystalline c-axis. The field produced should be uniform over the desired frequency region of 20 to 100MHz. This eliminates the possibility of using high "Q" conventional tuned circuits. One possibility was to use a lumped transmission line equivalent as the sample coil. Using this configuration means that there will be a transition from coaxial to lumped and back to coaxial transmission line (Fig.7). This configuration should provide a uniform magnetic field over a broad range of frequencies because of the inherent broadband properties of coaxial lines. A prototype was designed, constructed and tested. Uniform low loss transmission was obtained over the desired operating frequencies.

Sample Preparation For Optical Data Storage Experiments:

A great deal of interest is being shown in the storage of data in solids. Data storage capability even in a small volume, e.g. 1 cm cube, can be extremely large when you consider the total number of atoms and the ability to access and address these atomic clusters by means of a focused laser beam of variable intensity and wavelength. Theoretically, data storage capability is on the order of 10^{10} kb/cc.

Previously obtained samples, although semi-functional, have cosmetic problems, limiting their usefulness. These blemishes consist of internally trapped air bubbles and poor surface quality. Ideally these samples should be optically flat and the material itself free of air bubbles or foreign matter. Any optical imperfections will result in poor data recovery.

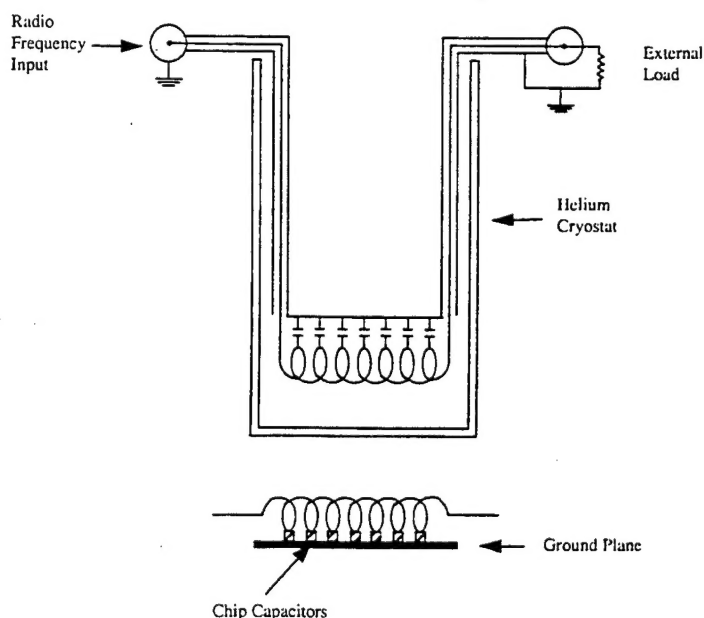


Figure 7. The configuration to observe the nuclear resonance in these rare earth ions.

The polystyrene host material received by us from the supplier came in the form of solid, random sized broken, air filled chip. It was now a question of converting these pieces into optical quality flats. The first attempt at removing the air bubbles was to grind the chips into a fine powder and then process this powder. This proved to be very time consuming and the amount of material obtained was too small to be useful. The next approach was to melt the polystyrene in a vacuum chamber and remove the air bubbles from the material. A stainless steel vacuum chamber with an external heater was constructed.

The initial heating of the polystyrene was done in the atmosphere so that a dopant could be thoroughly mixed into the molten mixture. This resultant mixture was poured into a boat and inserted into the vacuum oven. The oven was sealed and then pumped to approximately 20 microns. As the system temperature approached the melting point of the polystyrene there was a significant pressure increase, partially due to the trapped air in the material and the unpolymerized polymer boiling out of the polystyrene. After allowing the mixture to cool, the boat was removed from the oven and the results looked very promising. The material was clear and free from any trace of bubbles.

Work on holographic storage material is being expanded to include room temperature memory storage materials. A storage device capable of operating at room temperature offers much more flexibility when being integrated into a piece of equipment. One promising host material is polymethylmethacrylate. All of the ingredients necessary to make this material are mixed and to the mixture is added phenanthraquinone, a key component dye. Polymerization of this mixture has to be carried out in a rigid baking sequence. In order to fabricate something useful, this mixture is poured into a mold. (Fig. 8). The mold is then placed into an oven and baked. Careful handling techniques of the materials had to be observed. Much of the preparation had to be done under a hood.

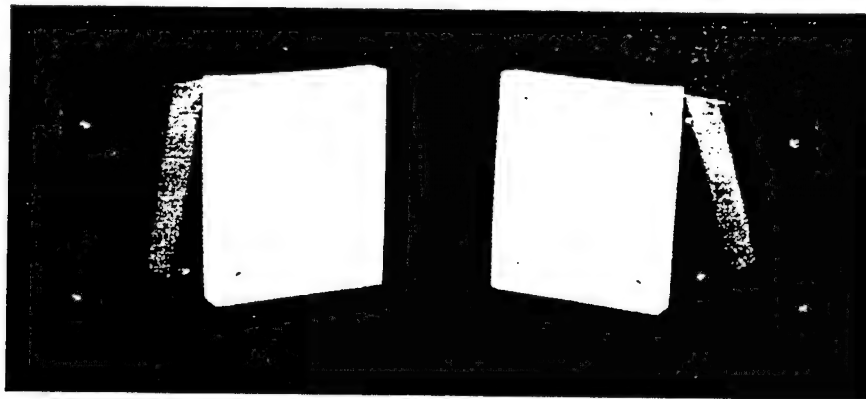


Figure 8. The mold for the three-dimensional holographic discs.

A fume hood was constructed for the bake-out oven to vent the gases produced during polymerization. All the materials necessary for the fabrication of three-dimensional holographic discs have been acquired and many trial runs have been made. In order to achieve the maximum storage capacity the finished discs must be optically flat, parallel and the material itself free from any microscopic bubbles and particles, which would increase scattering and reduce the resolution. The size of the discs that are being made is 50mm diameter and 3mm thick. In order to make optically flat discs it is necessary to start with two optical flats (1/10λ or better). These

two flats are imbedded in separate halves of a split mold with a flat separation equal to the desired disc thickness. The mold material is Teflon, which is inert in the presence of the corrosive polymer mixture. These two Teflon mold halves are then sandwiched between two aluminum plates. This mold design allows a great deal of flexibility when removing the finished disc and assembly for further use.

The chemistry necessary for the preparation of the polymer consists of mixing the appropriate amounts of monomer, polymer, dye and initiator. All of the above have to be performed under a suitable fume hood, as some of these chemicals are extremely noxious. After the addition of the dye further steps are carried out in the dark, since the material has now become photosensitive. The solution is now ready to be poured into the oven and baked. Early results were far from satisfactory as the polymerized discs had many bubbles. This problem had to be solved, as the presence of these bubbles made the discs unsatisfactory for use. The maximum temperature in the baking process is close to the boiling point of the monomer. In order to separate these temperatures it was necessary to construct another oven which can be pressurized, thereby increasing the boiling point of the monomer. This solved the problem and samples that are free of macroscopic bubbles are now being produced.

Until the present time fabrication of holographic samples has been limited to a single sample. One of the limitations has been oven space. A larger oven has been constructed and tested. Measurements have been taken to determine the homogeneity of the internal temperature of the oven. The oven now has the capability to bake five or six samples at a time. Another problem that had to be solved was controlling the temperature during the baking cycle. The entire baking schedule extends over a 30 to 40 hour period. At various times during the baking cycle the temperature is stepped up and down. This means that someone had to be there physically to change the temperature at usually awkward times. A microprocessor based temperature controller has been installed, which will step the oven through the required steps automatically in a hands-off fashion.

A new mold configuration is being designed. Although the original mold was capable of producing samples, the mold has many problems. Polymerization of the seepage around the optical flats makes it difficult to remove the samples. The problem has been partially solved by making close fitting caps, which go around the optical flats, making a tighter seal with the mold.

Time has been spent working on the electronics used to synchronize the operations involved in writing a series of holographic images. Specifically, digital circuits controlled by instructions from a computer, controls the sequence of events that include loading an image, changing the angle on the galvanometer and opening the shutter in front of the laser. A counter and an R-S flip flop were used to stop the process after 128 images are written in a single spot.

Supersonic Beam Component Construction:

Assembly has begun on a fairly large supersonic beam apparatus. This apparatus will produce a nearly monochromatic, high flux beam of rubidium atoms. This source of atoms will be used for performing experiments in near-resonant non-linear optics, such as optical phase conjugation. A picture of the finished system is shown in Fig. 9. One of the key elements in producing a supersonic beam is the collimating skimmer shown in Fig. 10. The function of this skimmer is to accept on-axis atoms and deflect off-axis atoms. The skimmer is constructed from a solid piece of copper. The cone angle is sixty degrees and the aperture at the apex has a diameter of forty mils.

The skimmer is preceded by an assembly of the nozzle and the primary skimmer. This assembly was constructed such that in situ alignment can be performed. A suitable control system had to be designed and constructed to provide fail safe operation for this system, which includes three mechanical and three diffusion pumps simultaneously. This system has maximum protection in case of a water failure. A water manifold was also constructed for the distribution of the cooling water.



Figure 9. The new supersonic beam system.

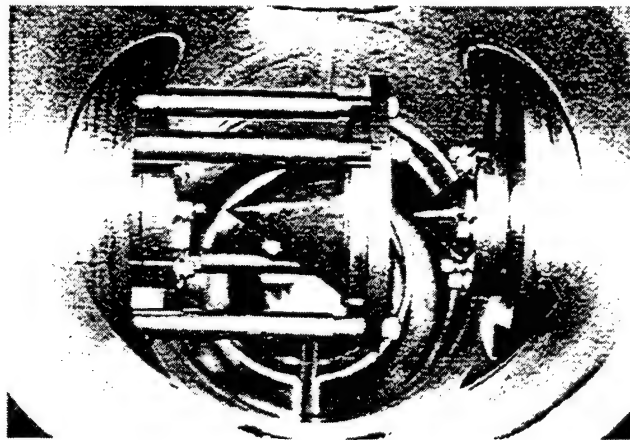


Figure 10. The collimating skimmer.

The electrical wiring and the cooling systems have been checked out and preliminary measurements have been performed on the vacuum system. The system had to be run in order to determine whether or not the Varian VHS10 diffusion pump has enough pumping capacity to maintain a sufficiently low pressure in the presence of a 1 atmosphere propelling gas. The tests were successfully completed. The next step was to design and construct two slits, which would be placed in the vacuum system. The position of these slits is shown in Fig. 11. These slits would

be used to further define the beam. The fixed slit is placed after the second skimmer and the variable slit a meter away from the first. The first slit assembly consists of a fixed slit, (dimensions, 3mm x 10 microns) mounted in the vertical direction. The second slit has to be rotatable in order to be aligned with the first. This adjustment has to be external to the vacuum chamber and is accomplished by mounting a Varian linear motion feed through on the side of the vacuum chamber. The linear motion is then converted to rotary motion on the ball bearing mounted slit Fig. 12. The slits are visually aligned and the final alignment is done with the aid of a laser.

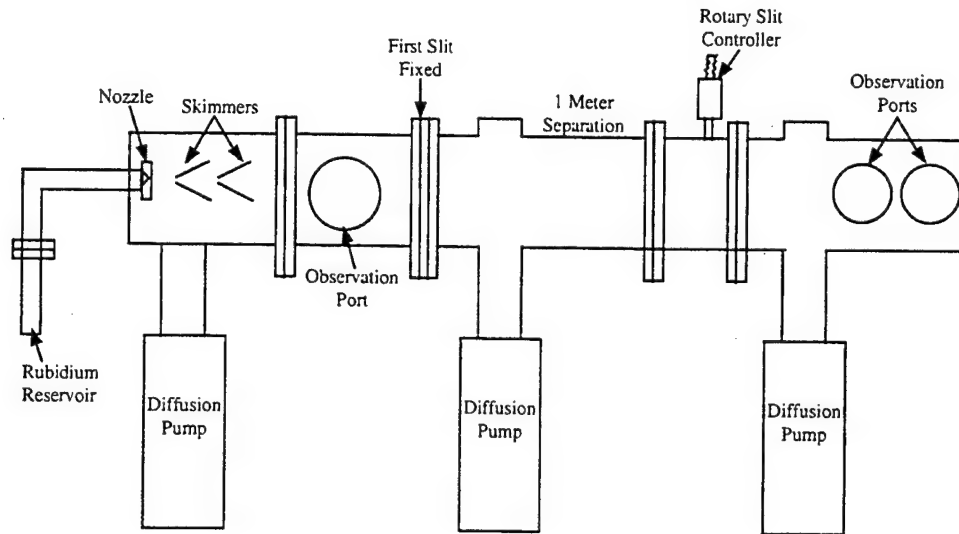


Figure 11. Illustrates the position of the two slits in the vacuum system.

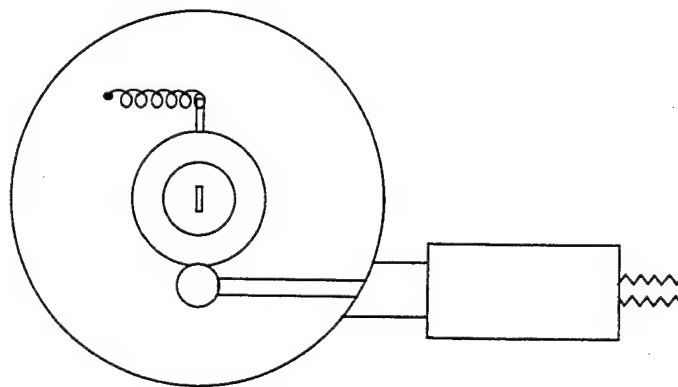


Figure 12. The ball bearing mounted slit.

At this point in the construction of our supersonic atomic beam apparatus, a detector capable of detecting small quantities of photons will be required. Photons will be emitted from the ultrasonic beam excited on resonance by a Ti-sapphire laser. A dry ice cooled, photomultiplier assembly, manufactured by Products for Research Inc., was mounted in a vertical position directly above one of the viewports at the end of the beam apparatus. In order to achieve the

highest detection efficiency, the imaging optics had to be installed inside the vacuum system in close proximity to the ultrasonic rubidium beam. Two large diameter lenses were mounted, one over the other, in order to obtain the correct focal length to image the light on the photodetector cathode and the output displayed on an oscilloscope.

Cryostat Setup:

Various materials have been investigated for memory storage applications. The materials that are currently being researched require cryogenic temperatures, and hence the need for a low temperature cryostat. The installation of a Janis SVT300 cryostat has been completed. This cryostat can be used over a wide range of temperatures from 1.5°K to 300°K. Pictures of the present setup are shown in Figs. 13 and 14. In order to make this system functional it was necessary to provide a vacuum system with adequate pumping capabilities, gas and cryogenic handling systems and temperature and pressure measuring equipment. Modifications had to be made to the sample head to accommodate the new samples.

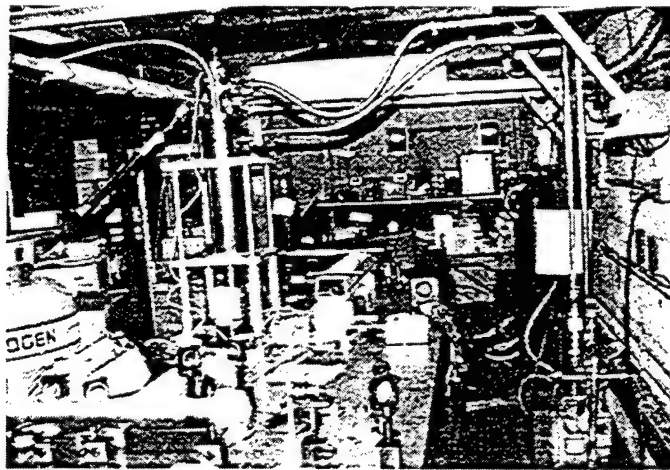


Figure 13. The cryostat setup.

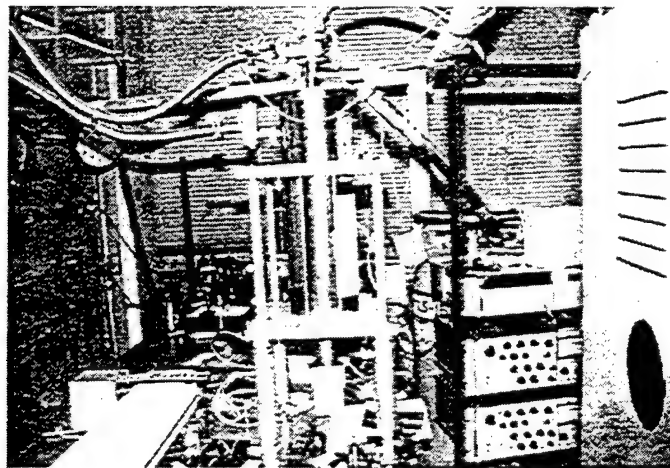


Figure 14. A close up of the cryostat setup.

A variety of materials are being investigated for possible use as the host material in a preliminary optical memory experiment. In order to obtain information from these samples, it is necessary to mount them so there would be optical access to the sample as well as providing radio frequency excitation. After considering a few options, it was decided that a microstrip configuration offered the best possibilities. There are now two cryogenic heads constructed, one for a powder sample and the other for a solid sample (diamond). Both samples are mounted in a microstrip configuration, that is, a current carrying conductor mounted over a ground plane and the samples sandwiched between the two electrodes.

The frequency of interest for these experiments lies between 1 and 18 GHz. Care has to be taken to avoid any abrupt discontinuities in the structure, with resulting non-uniform response over the desired frequency range. Optic access to the diamond sample material is obtained by drilling two 0.020" diameter overlapping holes, one in the microstrip and one in the ground plane for light transmission and one in the microstrip for the powder sample to observe the reflected signal. (Fig. 15, 16 and 17.)



Figure 15. Microstrip heads for mounting powders and diamond.

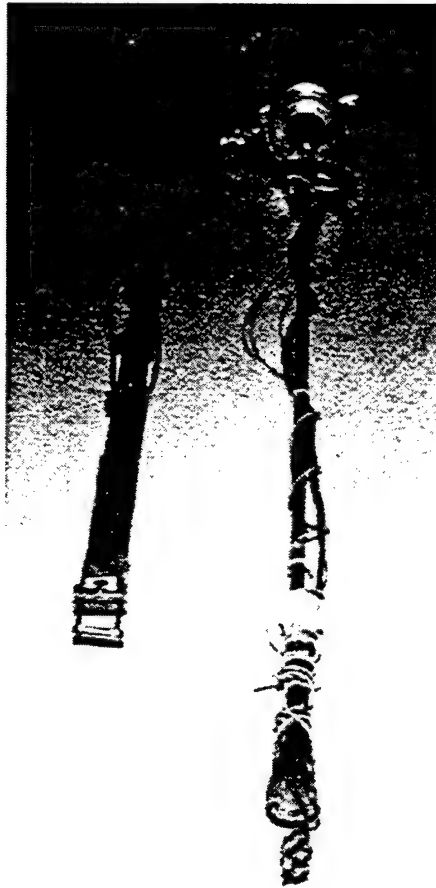


Figure 16. Full view of microstrip heads.



Figure 17. End view of microstrip heads.

TECHNICAL ACTIVITY:

My responsibilities on this contract range from basic equipment maintenance to process development of InP-based high photonic components, such as high electron mobility transistors (HEMTs), metal-insulator-semiconductor field effect transistors (MISFETs), and Metal Semiconductor Metal photodetectors (MSMs).

Process Developments:

Our HEMT and MISFET wafers are grown by molecular beam epitaxy by an outside source. Fig. 1 illustrates the epitaxial structures for each device.

N+ InGaAs (10nm)	InGaAs (30nm)
InAlAs(40nm)	Inp(25nm)
AtomicPlanar Doping	InGaAs (75nm)
InAlAs (5nm)	InP(4nm)
InGaAs (30nm)	SI InP Substrate
InAlAs (200nm)	
SI InP Substrate	

Figure 1. The epitaxial structures for each device.

MISFETs:

SNHC has been working on InP-based MIS structures. The main problem with these structures has been finding a suitable insulator to keep gate leakage to a minimum. Several experiments using thin layers of evaporated Si followed by a low temperature oxide were performed. The most promising results have been from the incorporation of a thin CdS layer followed by a low temperature SiO₂ deposition. These results were presented in the Indium Phosphide and Related Materials conference in Germany. The process consists of:

1. MESA (PR mask, wet chemical etching of unmasked material)
2. Recess (PR mask, recess etch, CdS Treatment ~50Å, Oxide Cap 1KÅ)
3. Gate (multi-layer PR mask, metalization, lift-off)
4. Ohmic (multi-layer PR mask, oxide holes, CdS holes, metalization, lift-off)
5. Anneal (350°C for 24 hours).

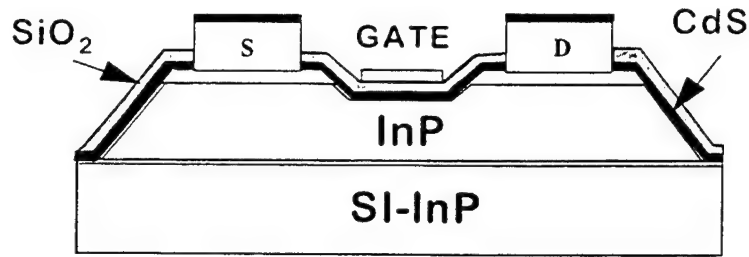


Figure 2. An illustration of a completed MISFET.

Due to the excellent insulating properties of CdS, it was decided to incorporate it into the HEMT process.

HEMTs:

SNHC has proven that good HEMTs can be made by using a three step process consisting of a mesa, ohmic, and a self aligned recess/gate metalization. SNHC is very interested in incorporating metal-semiconductor-metal detectors (MSMs) with our already proven HEMT technology; therefore a more involved process is needed to allow this incorporation to take place. A new process was devised and much work has been done to take that process to the next level. This new process not only offers a passivated surface for the subsequent mounting of MSM detectors, but also incorporates current CdS surface passivation technology into the process to improve Schottky barrier formation. The process consists of:

1. MESA (PR mask, wet chemical etching of unmasked material)
2. Passivation ($\sim 50\text{\AA}$ CdS followed by $1\text{K}\text{\AA}$ SiO_2)
3. Ohmic (multi-layer PR mask, oxide holes, CdS holes, metalization, lift-off)
4. Second Oxide for Passivation ($1\text{K}\text{\AA}$ SiO_2 , ohmic anneal)
5. Recess (PR mask, oxide removal, CdS removal, recess etch)
6. Second CdS Treatment ($\sim 50\text{\AA}$)
7. Gate (multi-layer PR mask, metalization, lift-off)

The previous steps are illustrated in figs. 3-5:

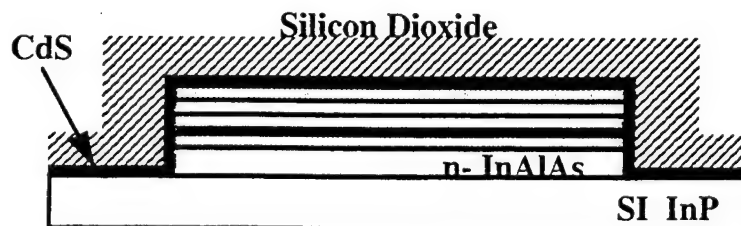


Figure 3. Steps 1-2

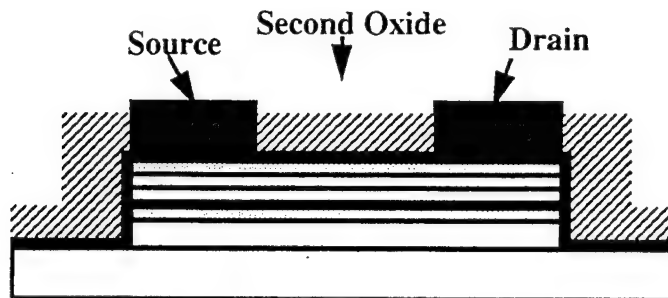


Figure 4. Steps 3-4

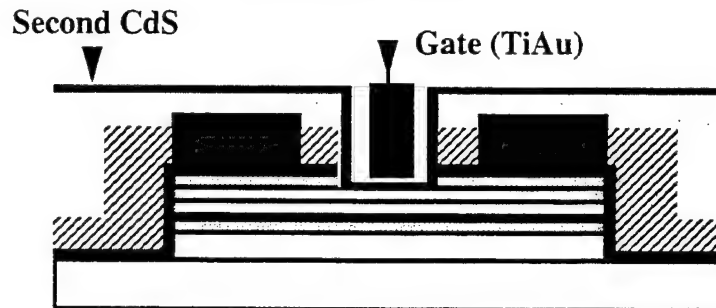


Figure 5. Steps 5-7

Illustration of completed HEMT

Several changes were made in the process; the most significant change has been the elimination of the thiourea pretreatment prior to the second CdS deposition. It is believed the thiourea attacks the exposed InAlAs that is needed for the Schottky barrier formation. Thus far, SNHC has demonstrated that good HEMTs can be produced using the above process. The next step is to design a mask set that will allow for the mounting of MSM detectors.

HIGFET

InP spacer 4.5nm	25nm ($n^+=4 \times 10^{18}$) InGaAs
	10nm (<i>undoped</i>) InP
	20nm ($n=5 \times 10^{17}$) InP
	40nm InGaAs Channel
	300nm InAlAs Buffer
SI-InP	

Figure 6. The epitaxial structure of a HIGFET wafer.

Another device interest is the HIGFET. Given its structure, several process issues had to be addressed. The first issue was the mesa etch. Since SNHC is not yet equipped with a plasma etcher, wet chemical techniques had to be used. After consulting with our engineers it was decided to use an etch that consisted of hydrochloric acid, phosphoric acid, hydrogen peroxide,

and DI water. Several different ratios of the acids were examined but we were never able to get vertical side walls. It was then decided to selectively etch each layer. After several attempts using the selective etches, accurate etch rates were determined, and this proved to be a very repeatable technique. The next issue was to be able to put enough metal on the device to run up the mesa. After several experiments, 4500Å seemed to be the correct number. Since so much metal was needed to raise the mesa, lift-off became a problem. To overcome this, experiments were performed using very thick single layer resists, multi-layer resists, and even image reversal resist. Even etch off techniques were examined. The best results came from using a double layer resist process. During these experiments, a sample mounting device was designed to perform metal evaporations at different angles to insure that metal would run up the mesa structures.

The insulator in these HIGFETs is the same as the MISFETs described previously. The process of using a chemical bath deposition of CdS followed by a low temperature oxide (SiO_2) is still being used. Several devices were processed using different oxide thickness. Data shows that the thinner oxide devices (~600Å) yield higher gain, but the thinnest oxide devices (~300Å) had metal adhesion problems. It is believed this is due to the CdS diffusing through the SiO_2 , leaving an undesirable surface.

Mask Design:

The design of a new mask set that would allow the integration of MSM photodetectors with HEMT transistors is complete.

As far as HIGFETs and MISFETs are concerned, the main process remained constant with slight variations in the CdS deposition step. The most significant variation to the CdS deposition process is the introduction of an ultrasonic bath. It is believed that the ultrasonic bath enhances CdS growth in the small 1µm features common on all of SNHC's devices. Device results show that the introduction of the ultrasonic bath has increased device performance on some of the smaller gated devices.

The mask set designed during the second quarter that allows MSM detector and HEMT circuit integration arrived; therefore, device processing changed back to HEMTs. Previous data was studied to discover which wafer gave the best performance and the three step process to test the new mask set was started. Data proved consistent with earlier results so the full process was started, which leaves the entire surface passivated to allow for the subsequent attachment of the separately processed MSMs. Upon completion, several circuits were tested across the sample and all worked well. Now it is time to mount the MSM detectors.

It is known that mounting 50µm x 50µm detectors is no simple feat. It is important to do one step at a time. The first step was to make a passivated HEMT circuit. The second step was to make detectors. Now comes the difficult task of bringing the two devices together. The MSM detectors are processed and then epoxy is used to mount the detector face down onto a glass slide. After mounting, a chemo-mechanical process is used to remove the substrate. Once the substrate is removed, all that remains is the detector itself isolated by epoxy (as seen in the illustration below).

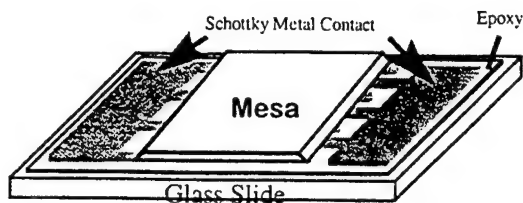


Figure 7. The detector isolated by epoxy.

In order for the HEMT-MSM integration to occur, it is necessary to remove the host substrate, in this case a glass slide, from the detector. It was decided that the easiest way to do this is to remove the mounting epoxy. Experiments were performed using different types of epoxies such as water soluble, UV curable, etc. These epoxies were not able to withstand the vigors of the chemo-mechanical substrate removal. Instead of continually trying new epoxies, the effort was concentrated on finding a technique to remove the epoxy used in the past. Several experiments using UV ozone and O_2 plasmas for the epoxy removal were conducted. It was discovered that the introduction of a low power O_2 plasma breaks down the epoxy and allows it to be rinsed away with DI water. The next step will be to find a suitable substance that will allow the alignment and attachment of the MSM detectors to the host HEMT circuit.

Anneal Study:

An anneal study was performed in order to determine the optimum anneal time and anneal method for SNHC's MIS structures. A large substrate was processed and then cut into 10 samples all approximately 1 cm^2 . Samples were annealed in both a conventional tube furnace and a rapid thermal annealer, varying both temperature and time. It was determined that anneals greater than 3 hours in the conventional tube furnace gave the best results whereas anneals in the RTA offered no promising results. When comparing results of samples processed between 3 and 20 hours it was concluded that sample quality increases with longer anneal times, but between 4 and 24 hours no significant increase occurs. We now use a 4 hour anneal in the conventional furnace.

More Device Processing:

Device processing this time was aimed toward MSM-HEMT integration. Work has been done in this area for some time and the new mask set is complete. Older material was used first rather than the expensive HEMT and MSM wafers to test the feasibility of this integration. This material wouldn't produce the best results but would still function and allow the devices to be tested to see if the integration worked.

For the HEMTs a simple three step process was used consisting of a mesa, ohmic, and a self aligned recess/gate metalization. This circuit was then passivated with a low-temperature SiO_2 cap to allow for subsequent mounting of the MSM devices. Transistor testing performed across the wafer yielded good I-V characteristics as shown in Fig 8.

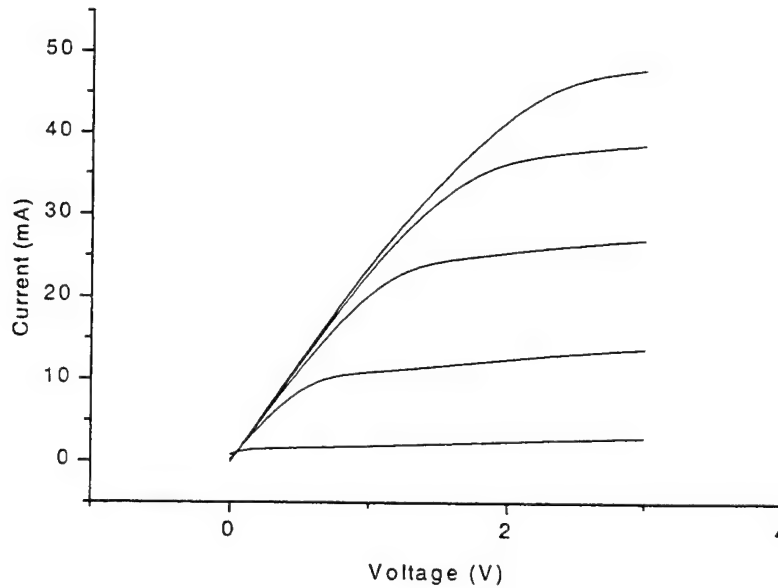


Figure 8. I-V characteristics

The HEMT circuit was then cut into several pieces measuring 2 x 1 cm. These passivated HEMT circuits were then epoxied face up to glass host substrates.

The MSMs were processed by patterning the schottky metal contacts, using a lift-off procedure. The MSMs were then attached to a 4 x 4 inch blank photomask using a small amount of photoresist.

The passivated HEMT circuit was loaded into the chuck of the HTG contact aligner. The patterned MSM attached to the blank photomask plate was loaded onto the mask holder of the contact aligner. IR alignment of the two wafers was performed, but only in proximity mode. The sample was lowered, making sure not to change the rotation or lateral movement of the sample. A small amount of the epoxy was applied to the surface of the HEMT circuit and the sample was raised back into position. The alignment was checked and adjusted and the aligner was put into contact mode. The sample was heated on the chuck for 5 minutes and then placed into a 90°C oven for 20 minutes.

After the epoxy cured, the entire sample was placed in acetone and the 4 x 4 inch photomask removed. The following is an illustration of the sample at this step.

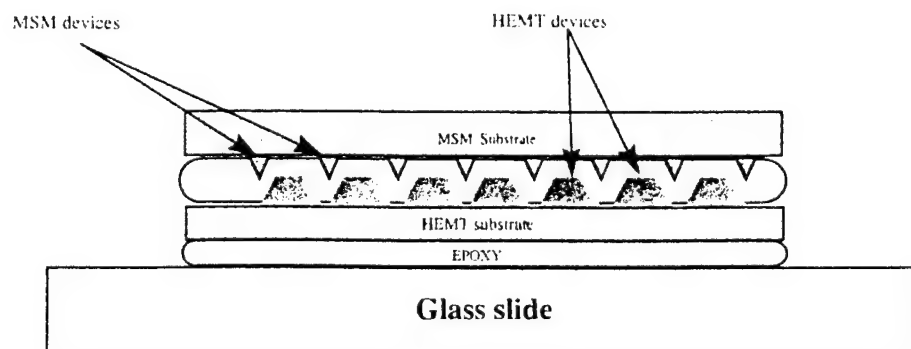


Figure 9.

The MSM substrate was removed by a chemo-mechanical process. A mesa was then patterned on the sample, which left only MSM detectors embedded in the epoxy.

The next step was to remove all unwanted epoxy and electrically connect the two samples. Several attempts were made, none of which were entirely successful. The biggest problem was the 50 μ m space between the HEMT and the MSM. The original plan was to do a simple evaporation to connect the two. The next attempt to connect the two is to try plating or bonding.

RIE of SiO₂:

The MISFET processing technique requires an SiO₂ etch prior to surface passivation of the material where the gate will be deposited. Since this etch is for gates with a length of 1 μ m, it is rather critical. Previously BOE was used to perform this etch with unrepeatability results. Sometimes the etch would not remove the oxide and sometimes it would overetch and undercut into the ohmic contacts. An experiment was set up to determine the etch rate of SiO₂ using a CF₄ dry etching technique. Results have proven this technique to be very repeatable, and it is now part of the standard process.

CdS Paper:

The success of silicon is largely due to the availability of CMOS technology, which is made possible by the nearly perfect electrical and chemical properties of the oxide/semiconductor interface. Conversely, the lack of an adequate surface passivation technology for the III-V semiconductors has severely curtailed analogous MIS device technology development, restricting the options for compound semiconductor circuit design. Recently, SNHC has developed a cadmium sulfide-based surface treatment that results in a chemically stable (100) *n*-InP surface, with nearly ideal MIS diode *C-V* response.¹ Despite the fact that the CdS deposition process is simple and can be easily integrated into many manufacturing processes, the interface chemistry of the CdS/InP system is complex. We will present a detailed analysis of the CdS/InP interface and suggest how the CdS passivation process can be extended to MISFET and HIGFET fabrication in III-V systems.

We have shown that sulfur fills phosphorus vacancies at the InP surface after a thiourea/ammonia pre-treatment, which is performed by immersing an unetched *n*-InP sample in a 20 ml solution of 0.033 M thiourea and 12.3 M ammonia at 85°C for 15 min.² The sample is then transferred to a CdS growth solution of 0.028 M thiourea (CS(NH₂)₂), 0.014 M cadmium sulfate (CdSO₄), and 11 M NH₃ for 3 min at 85°C. MIS samples were prepared by subsequently depositing 300 Å of SiO₂ at 3 Torr and 260°C. After thermal evaporation of Al front contacts and In back contacts, samples were annealed overnight in N₂ at 350°C. The 1 MHz and quasistatic *C-V* response curves for a sample prepared as described are shown in Fig. 1(a). The response of the sample is nearly ideal at 1 MHz and exhibits exceptional low frequency response from accumulation to inversion, clearly demonstrating that the Fermi level is unpinned. The theoretical *C-V* response is shown for both 1 MHz and quasistatic by the open circles. *C_{min}/C_{ox}* for the quasistatic curve in Fig. 1(a) is 0.26, compared to the theoretical value of 0.13. The *D_{it}* values for

¹ H.M. Dauplaise, K. Vaccaro, A. Davis, G.O. Ramseyer, and J.P. Lorenzo, "Analysis of thin CdS layers on InP for improved metal-insulator-semiconductor devices," *J. App. Phys.*, vol. 80, pp. 2873-2882, Sept. 1996.

² H.M. Dauplaise, A. Davis, K. Vaccaro, G.O. Ramseyer, and J.P. Lorenzo, "Analysis of InP Passivated with Thiourea/Ammonia Solutions and Thin CdS Films," *MRS Symp. Proc.*, vol. 448, to be published April 1997.

the samples are shown in Fig. 1(b). Interface-state densities were calculated by the method of Castagné and Vapaille, using both high-frequency and quasistatic C-V data. The calculated minimum interface-state density was typically $1 \times 10^{11} \text{ eV}^{-1} \text{ cm}^{-2}$ for CdS-treated MIS samples.

Figure 2(a) shows the S 2*p* spectrum for an InP sample that has been pre-treated in a thiourea/ammonia solution, followed by deposition of a thin CdS film for 3 min at 85°C. The sample was analyzed before and after heating in vacuum for 1 hour at 200, 300, and 400°C in order to assess the film stability as a function of temperature. The S binding energy is 161.8 eV, and can be attributed to a sulfide, but a small sulfate signal is also seen at 164.8 eV. The sulfate component is removed by annealing at 350°C. Figure 2(b) shows the Cd 3*d*_{5/2} peak of the sample in Fig. 2(a); the binding energy is 405.1 eV. This value agrees well with previously reported data on single-crystal and thin-film CdS samples. It is evident from Fig. 2(b) that, following annealing at 300°C, the Cd signal is no longer detected. There is also a corresponding decrease in the S signal. The evolution of Cd from the sample suggests that the Cd compounds are not strongly bonded to the substrate. Figure 2(c) shows the P 2*p* peak for the sample. We see no evidence of P-S or P-O bonding. The In 3*d*_{5/2} peak, Fig. 2(d), is similar to that of a pre-treated sample. Again we see that a sulfide component is present for the In 3*d*_{5/2} peak. This data indicates that, in addition to the sulfur bound to cadmium, which is expected, a significant fraction of the sulfur at the InP surface is bound to indium.

Deposition of a thin layer of CdS yields dramatic improvements in MIS C-V response. In-S bonding is observed with XPS, and samples with the deposited CdS layer also exhibit higher P/In(-P) ratios. Pre-treated samples with or without a subsequent thin CdS film showed no evidence of native oxides at the surface. The CdS layer may also serve to protect the In-S layer during dielectric deposition, but it is unstable when unprotected at temperatures between 300 and 350°C. Both InP MISFETs and HIGFETs have been fabricated using this sample passivation technique. For the first time, InP depletion-mode MISFETs with channel pinch-off, saturated I_{DS} , and gain have been fabricated using this process and will be presented.

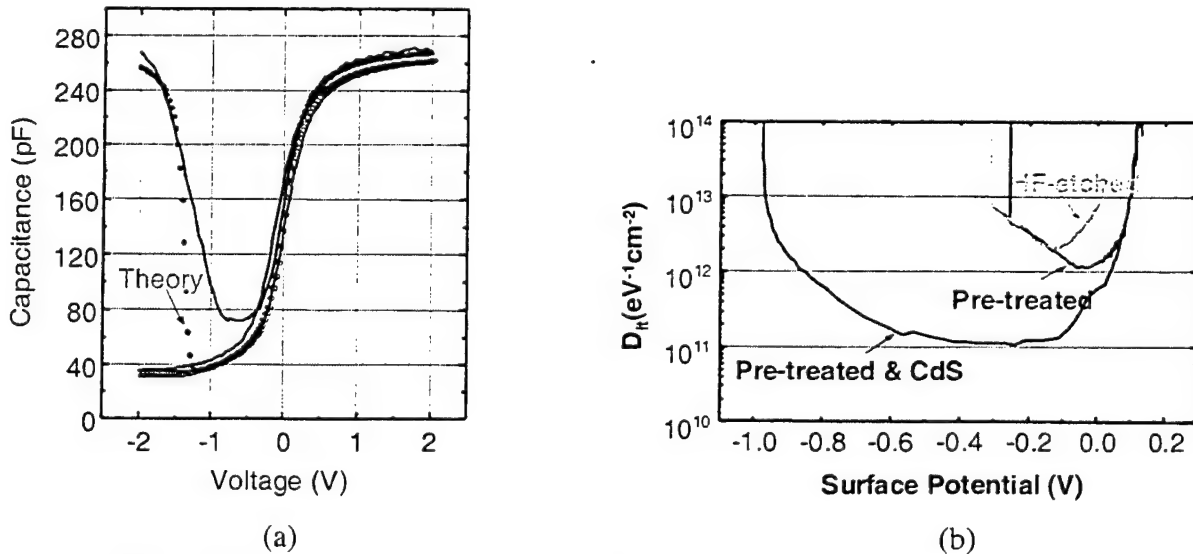


Figure 1. (a) The 1 MHz and quasistatic response of an *n*-InP MIS sample prepared with a thiourea/ammonia pre-treatment and an $\sim 30 \text{ \AA}$ CdS layer. The theoretical 1 MHz and quasistatic responses are indicated by the open circles. (b) D_{it} values for the sample shown in (a) and for HF-etched reference and pre-treated samples.

Process improvements thus far have been the design of a new mask set, as well as new implant specifications. An account was set up with Implant Sciences to allow us to provide them with substrates and implant specifications and in a few days we receive the implanted wafer. The plan is to get implants on SI InP as well as n-type. The n-type wafers will be used in implant characterization experiments while the SI wafers will be used to make the devices.

Several detector bonding experiments were performed. Early results show the mounting epoxy does not serve as a hard enough surface for ultrasonic wedge bonding. Future experiments will consist of the sputtering of AlO_2 over the detector prior to host mounting. This experiment is to see if the AlO_2 will be rigid enough to handle the bonding. Harder epoxies will also be investigated.

Research began with several sulfur implants on both semi-insulating indium phosphide as well as n-type indium phosphide. These wafers were blanket implanted, meaning the entire surface was bombarded with sulfur ions. The different implants are listed in the table below.

Sulfur Implants On Semi-insulating &
n-type Indium Phosphide
WAFER 1 & 2 respectively.
Sulfur Implants On Semi-insulating &
n-type Indium Phosphide
WAFER 3 & 4 respectively.

25KeV	$1.0 \times 10^{13} / \text{cm}^2$
75KeV	$7.5 \times 10^{11} / \text{cm}^2$
100KeV	$7.5 \times 10^{11} / \text{cm}^2$
25KeV	$1.0 \times 10^{13} / \text{cm}^2$
75KeV	$7.5 \times 10^{12} / \text{cm}^2$
100KeV	$7.5 \times 10^{12} / \text{cm}^2$

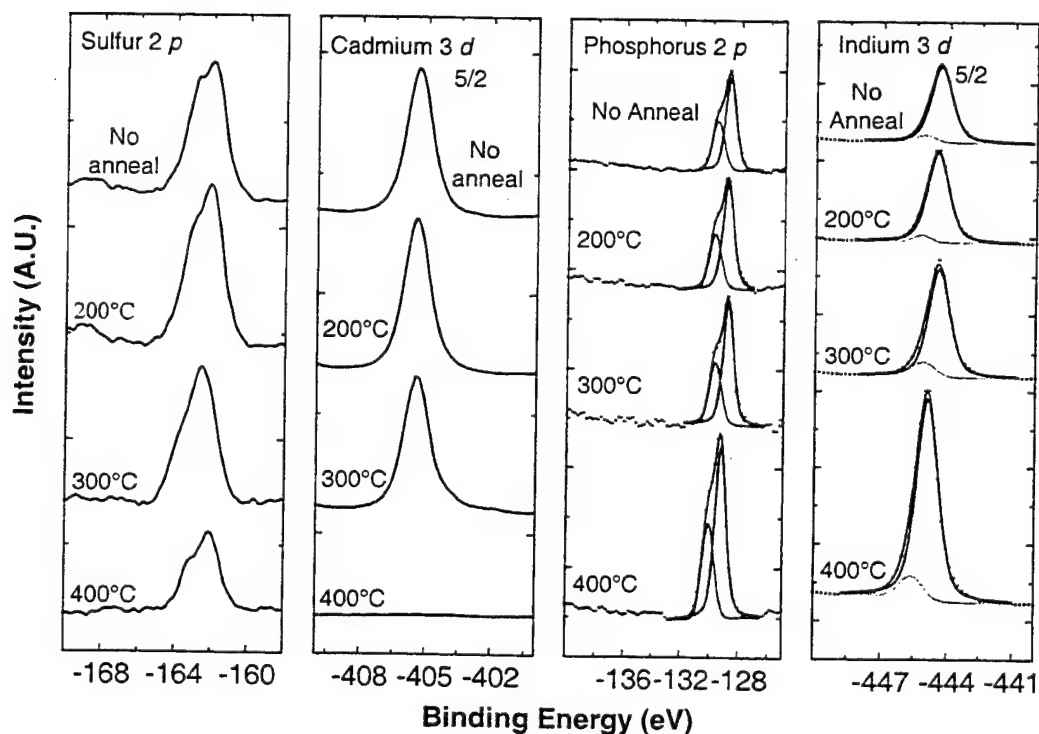


Figure 2. The (a) S 2p, (b) Cd 3d_{5/2}, (c) P 2p, and (d) In 3d_{5/2} detail scans of a pre-treated n-InP sample with a thin CdS film unannealed and after anneals at 200, 300, and 400°C. The dotted curves in (c) are for the 2p_{3/2} component, while the dashed curves are for the 2p_{1/2} component. The bulk component, In(-P), for the In 3d_{5/2} peak in (d) is shown by the dotted curve, and the In(-S) component by the dashed curve.

Different implants are important for research purposes but equally important were the implants performed on the n-type wafers. There were implants performed only on semi-insulating wafers which are required for the actual device processing, but when carrier concentration as a function of depth measurements were performed on these wafers very little data was obtained. This was because once a few hundred angstroms of material were removed from the surface, so were all the carriers. Having n-type wafers implanted along side of the semi-insulating wafers offers an invaluable tool for the characterization of the implant as well as the activation. Having n-type wafers implanted makes it possible to measure the carrier concentration as a function of depth right down to the substrate, which has a known carrier concentration.

Now armed with the right tools for the right experiments, we started. The first and most vital step was to decide the correct activation anneal. The samples were capped using a combination of sulfur and SiO₂ and then annealed as illustrated in the table below.

<u>Anneal Temperatures / time</u>	<u>Surface Carrier Concentration</u>
725°C / 300s	5.48 X 10 ¹⁸
725°C / 60s	7.69 X 10 ¹⁷
775°C / 10s	8.59 X 10 ¹⁷
850°C / 10s	9.75 X 10 ¹⁹
800°C / 10s	7.64 X 10 ¹⁷

Several anneals were performed and carrier concentrations measured. The instrumentation used to measure the carrier concentration was a polaron manufactured by Bio-rad. The system uses an indium back contact and an electrolyte for the front contact. From the data above, at first glance it looks like the 850°C for 10s anneal is the best. The measured carrier concentration is actually higher than the implant. This is due to surface damage. The anneal that produced the best, most repeatable results was the 725°C for 300s. This anneal left the wafer with no cracks, and by the polaron characterization results, the best carrier concentration at the surface. Good results at the surface (**ohmic area**) are not the only concern. These devices also have a channel, somewhere around 200 angstroms below the surface. As shown in the implants, the energy levels vary. Low energy levels yield a shallow implant, while high energy implants yield a deep implant. The table below shows the carrier concentration 200 angstroms below the surface (**channel**). Calculations have shown the ideal carrier concentration at this depth; we hope we can measure these values as well.

<u>Anneal Temperatures / time</u>	<u>Channel Carrier Concentration</u>
725°C / 300s	9.41 X 10 ¹⁶
725°C / 60s	4.86 X 10 ¹⁶
775°C / 10s	4.97 X 10 ¹⁶
850°C / 10s	1.93 X 10 ¹⁷
800°C / 10s	4.18 X 10 ¹⁶

From the data listed above, the 725°C anneal still looks the best. More measurements were taken using a Hall/Van Der Pauw set up. While the carrier concentration seems acceptable, mobility is down by at least a factor of two when compared to the ideal.

Devices were processed and the anneal remained constant, but the channel recess etch was experimented with several times.

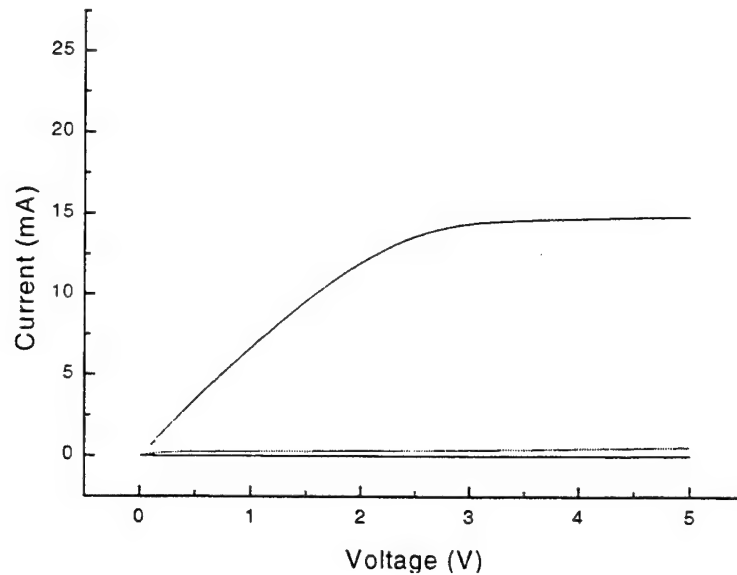


Figure 10. Typical IV characteristics for these MisFET's.

This batch of MISFETs are approximately twenty percent better than last quarters. The IV data shows the ohmic contacts still need improvement. If the ohmic contacts were better, the current would rise much higher in the Fig. 10. The next batch of implants have much higher doses near the surface, which should help the ohmic problem. The species have been changed for the third time. The implanting of Si started two quarters ago, S last quarter, and now Sn is the species of choice. The only problem with changing the dose, species, etc., is that all of the above experiments have to be repeated.

The major difference in these implants from previous is that some wafers had a single implant at high energy and at a low dose. This low dose/high energy implant leaves the ions well below the surface. Basically this is the same implant we used before for the active region of the device. One of the major limiting factors of our device performance is the surface damage due to the low energy/high dose implant used for ohmic contacts. This low energy/high dose implant leaves the surface badly damaged and it takes an anneal of a very high temperature to re-grow the sample. By eliminating or at the very least postponing this implant, the ions are well below the surface and when it comes time for activation the wafer can re-grow from both above and below the implant as seen in the following illustration.

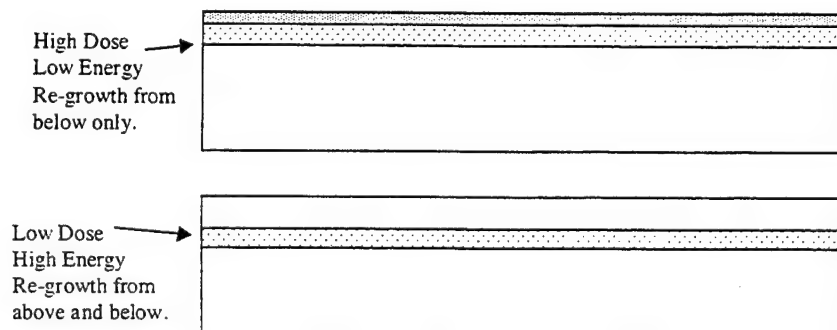


Figure 11.

The major problem with this particular set up is the elimination of the blanket ohmic implant. Without the ohmic implant, contacts would have a large resistance and it may be better off with the damage. Much time was spent on devising a new process which would give the best of both worlds. Several options are being proposed and all would need a new mask set. It was decided to go ahead and process these wafers and see if they behave better disregarding the high contact resistance.

A new approach of using the MBE grown CdS as the emitter material for an HBT device is being examined. Much time was spent testing the feasibility using the old mask set and some old MOCVD grown HBT wafers. The emitter metal has been put down. When the attempt was made to etch down to the collector, serious problems occurred. The proper wet chemical etch for this experiment has not been located thus far. A mask set will be designed to integrate the detectors with these new CdS HBTs.

Much time was spent trying to mount the high-speed photodetectors in a package. Several ideas were rejected and not much progress was made. Early attempts were to attach the detector directly to a 50 GHz bias tee. A new search is in progress for a ceramic substrate with microwave strip lines and a bias tee built in.

Equipment Maintenance:

- Preventative maintenance on SNH's semiconductor processing equipment.
- Due to building chilled water problems, installed 15,000 BTU recirculating chiller.
- Maintained e-beam evaporator in operational condition.
- Installed and qualified UV ozone cleaning system.
- Retrofitted UV Ozone system with temperature control unit.
- Troubleshoot H₂ purifier.
- Repaired resistivity meter for DI water system.

Computers:

Installed network hardware and software into SNHC's computer systems.

Ultra High Vacuum Evaporator:

Assisted engineers in the design of a UHV evaporator for thin film deposition. Consulted with various UHV suppliers to purchase as many as possible off-the-shelf components to keep costs to a minimum. Built, tested, put into operation.

Wedge Bonder:

Set up and qualified K&S 4123 manual wedge bonder. Packaged MIS structures for CV/GV analysis, and DLTS measurements.

Silicon Germanium Reactor:

Installed new dry diaphragm pump into gas handling system. Repaired and reinstalled Varian multigauge vacuum gauge controller.

Networking:

Delivery was taken of four P6's. Many hours were spent setting up hardware and software to meet SNHC's retailored computer requirements. All lab computers were set up to run both

Windows for Workgroups and Chameleon NFS network systems. With the exception of one, personal machines were set up with Windows NT.

Equipment Maintenance:

- Install, setup, and qualify RIE system.
- Install RGA filament in SiGe reactor.
- Replace transfer microswitch assemble in sub-micron contact mask aligner.
- Repaired TC in ultrasonic wedge bonder sample chuck.

Surface Analysis Room:

- Prepped room for set up of class 10,000 soft wall clean room to include everything.
- Set up frame, installed fans, lights, blanks, etc.
- Installed wet bench.
- Installed and co-designed HV CVD.
- Installed CDS MBE reactor.

Bonding:

- Packaged SiGe diodes, MIS structures for DLTS, and DC measurements.
- Bonded PtSi test structures for IR Surveillance Branch.
- Removed load-lock turbo pumping system on XPS.
- Installed turbo-drag pump with dry backing pump on XPS system.
- Designed new pumping scheme for longer life of load-lock pumping system.
- Rebuilt rotary vane pump.
- Regenerated all cryo-pumps.
- Started construction of UHV evaporator.
- Set up the UHV vacuum evaporator with palladium to give us other ohmic contact options.
- Installed thermal sources for Ni and Cr.
- Installed and programmed e-beam controller for pattern generation.
- Found supplier for drain pump and fixed clean room humidifier.
- Cleaned all DI water lines, tanks, and filter housings many times.
- Fixed vacuum leak on aluminum evaporator and cleaned system.
- Set up SEM.
- Retrofitted SEM for E-beam direct write.

TECHNICAL ACTIVITY:

All work was done in conjunction with AFRL/SNHX bulk crystal growth program to produce single crystals for opto-electronics applications and for substrates to be used in high temperature nitride based devices.

Sillenite crystals were grown by top seeded solution growth with enhanced nonlinear optical properties to better suite them as optical storage medium/image processors for target recognition and beamsteering applications. Also the photorefractive effect in hydrothermally grown bismuth silicon oxide was improved.

Zinc Oxide is a substrate candidate for nitride based devices and also has potential as a semiconductor material of its own. ZnO single crystals were grown hydrothermally with better uniformity and less defects. It was found that both conducting and semi-insulation zinc oxide substrates can be produced depending on the growth parameters and growth orientation. Initial studies were performed on how impurities, defects, and preparation affect the mechanical, electrical, and surface properties of zinc oxide.

Gallium nitride based devices are entering the developmental stage for commercial and military devices. Unavailability of GaN substrates limits functionality, production, and performance of these devices. Gallium nitride single crystals that were up 2.5mm x 8.0mm were grown by chemical vapor reaction. These crystals exhibited high photoluminescence and narrow rocking curves. Growth by ammonia solution did not produce any crystals but has the potential to grow large nitride based substrates.

Accomplishments:

Tasks were accomplished in five main areas: Growth of Sillenite single crystals by Czochralski TSSG (top seeded solution growth), growth of Sillenite single crystals by Hydrothermal solution growth, growth of zinc oxide single crystals by Hydrothermal solution growth, growth of nitride single crystals by ammonothermal solution growth, and growth of nitride single crystal by chemical vapor transport. Work accomplished is summarized in the table below.

	Number of Experiments Conducted	Crystals Produced	Enhanced Material Produced
Cz. TSSG Sillenites	80	70	YES
Hydrothermal Growth Sillenites	30	45	YES
Hydrothermal Growth Zinc Oxide	38	45	YES
Ammonothermal Nitrides	10	NONE	N/A
CVP Growth Nitrides	50 (closed or quasi) 20 (open)	mm size	YES

Table I: Summary of experiments conducted

Sillenite Czochralski TSSG Growth:

Experimental:

Bismuth silicon oxide, bismuth germanium oxide, and bismuth titanium oxide (BSO, BGO, BTO) single crystals were grown by top seeded solution growth (TSSG) using resistance dual chamber heated furnaces. They were grown at a temperature of 800-1050°C depending on the type of crystals. Different dopants (phosphorous, aluminum, manganese, magnesium, cobalt, vanadium, and others) of varying amounts were incorporated into the crystal in order to enhance various optical properties.

Results and Discussion:

There were approximately 70 crystals produced, 25 of which were BSO, 15 which were BGO, 10 which were BTO, and 10 which were sillenite crystals of mixed compounds. Most of the samples incorporated various dopants. The majority of dopants either degraded or slightly improved the optical and photorefractive properties of the crystals. George Fisher, previously an employee of AFRL, discovered that one of the crystals grown greatly improved both the gain and the decay time in a two wave mixing experiment. The crystal was a BSO crystal that was co-doped with manganese and phosphorous. A series of BSO, BTO, and BGO crystals were grown with manganese and phosphorous co-dopants and the results are summarized below.

Sillenite Material	Optical Gain*	Rise Time	Decay Time
Undoped BSO	100	10 ms	10 sec
Mg/P doped BSO	500	10 ms	> 2 hours
Undoped BGO	50	10 ms	10 sec
Mg/P doped BGO	250	10 ms	> 1 hour
Undoped BTO	1	10 ms	10 sec
Mg/P doped BTO	15	10 ms	> 1 hour

* Gain normalized to an undoped BTO sample

Table II: comparison of optical properties of various sillenite crystals

The picture below is of a read beam shown through a Mg/P doped BSO crystal in a two wave mixing experiment. As shown the holograph is clearly visible after five minutes of decay time.

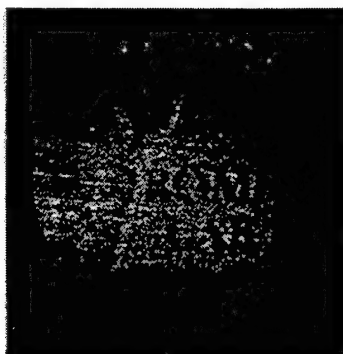


Figure1: Holograph read out of Mg/P doped BSO crystal

It was also discovered that all the crystals grown during this contract were left-handed. The sillenites have an optical activity of 20-25 degrees. Right handed samples rotate an incident beam clockwise whereas left handed samples rotate an incident beam counterclockwise. The majority of the crystals grown by other groups are right handed. Right handed seeds were obtained to grow right handed crystals, since some preliminary research is being done on applications requiring both left and right crystals.

Some research was also performed on growing BSO with excess bismuth but this met with limited success as it was hard to incorporate excess bismuth by melt growth. Bismuth iron oxide, BFO, was also grown but showed no photorefractive properties in the wavelengths that were measured. Combinations of $\text{BS}_x\text{G}_{1-x}\text{O}$, $\text{BF}_x\text{S}_{1-x}\text{O}$ were also attempted with no gain seen in the optical properties of these crystals over standard sillenite crystals.

Recommendations:

Further studies need to be performed on those crystals grown. Two wave and four wave mixing experiments need to be conducted at different wavelengths other than those measured. A study was just getting started on uniformity of the Mg and P dopants in a doped BSO crystal and the corresponding optical properties throughout the boule of BSO. Optimization of optical properties should be able to be accomplished by varying the amount each dopant incorporated into the crystal. There is also a problem of maintaining uniform levels of the dopants throughout the crystal. Work was starting on how to optimize the uniformity and effect of these optical properties throughout a grown crystal, when funds ran low to complete the study. A complete study should also be done into the solid state mechanisms that enhance these optical properties; this in turn will give better insight into how doping can best be accomplished.

Collaboration was initiated with the Manufacturing Directorate of AFRL at Wright Patterson AFB and Ian McMichael at the Rockwell Science Center to work on an Electro Optic Power Limiter concept for laser protection. Both left and right-handed BSO are used in the Power Limiter in order to cancel out optical activity, which degrades the efficiency of the Limiter. Both this and other applications need large, $>2''$, diameter crystals with low strain in order to reduce residential birefringence.¹ Research needs to be done in order to grow large left and right handed crystals with low strain by using better temperature and diameter control and other techniques.

Finally more research needs to be done on different dopants and more combinations of dopants. Some dopants degrade one optical property adversely (i.e. rise time) while enhancing another optical property (i.e. optical gain). Different applications require enhancement and/or degradation of different optical properties. A more complete dopant study on the sillenites would allow for optimization of devices, which contain these crystals.

Sillenite Hydrothermal Growth:

Experimental:

Sillenite single crystals (BGO, BTO, and BSO) were produced in 1" and 3" ID high strength steel autoclaves. Platinum liners were used because of the caustic nature of the solution (3-4N NaOH and/or KOH). Sillenite single crystal seeds, along with nutrients, and solvents were placed in the liner. The liner was then sealed by stick welding. The volume fill of the liner was between 70-80 percent and the proper amount of 1N NaOH solution was added on the outside of the liner to match the fill rate on the inside of the liner. The following procedures were used:

1. Nutrient preparations: Nutrient was either taken from TSSG grown crystals or from centered material. The Nutrient was then crushed into 3/8 to 3/4-inch pieces.
2. Seeds were cut out of TSSG runs or prior Hydrothermal runs in the $\langle 100 \rangle$, $\langle 110 \rangle$, or $\langle 111 \rangle$ direction.
3. Solvent: 4N NaOH was used in the BSO experiments. 3N NaOH and 1 N KOH were used in the BGO and BTO experiments. 0.1-0.25 N Li_2CO_4 was used in the later experimental runs to help promote seed overgrowth.
4. Duration: Run times were 35-41 days for the 1" autoclaves and 35-51 days for the 3" autoclaves.
5. Growth-temperatures: The growth temperature was 395°C with a $7^\circ\text{--}10^\circ\text{C}$ temperature gradient between the top and bottom zones of the autoclave. A schematic of the system is shown below.

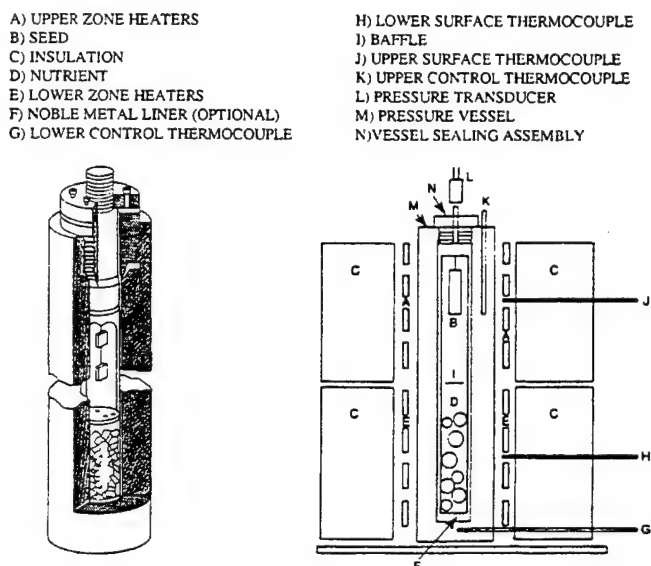


Figure 2: Schematic of autoclave system

Results and Discussion:

It was discovered that there is an initial low quality overgrowth near the seed interface. Lithium Carbonate was added in order to alleviate this problem but only improved the growth slightly. This initial overgrowth gradually improves until a high quality surface is reached. On a typical run 1-5 mm high optical quality plates can be cut from the crystal. A sampling of the plates grown is shown in Fig. 3.

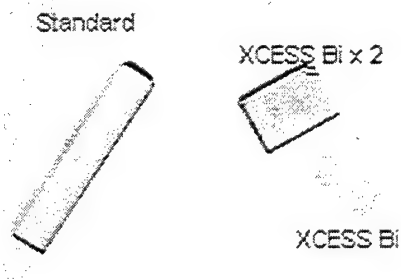


Figure 3: Hydrothermally grown plates

When standard BSO nutrient is used either from previously grown crystals or from casted BSO (melted at 950°C for 24 hrs.) the resulting hydrothermal crystals were clear in color and had no photorefractive (PR) properties (Standard in Fig.2). This hydrothermal material could then be broken up and re-grown by TSSG and would again have the typical straw color that BSO crystals grown from the melt have. This seems to indicate that a defect is incorporated into the crystal at high temperatures in the melt, whereas hydrothermally grown BSO does not have this defect and is nearly stoichiometric.² These clear plates were subjugated to gamma radiation with no adverse affects, whereas TSSG grown crystals were adversely effected by radiation. BGO and BTO hydrothermally grown crystals had a slightly yellowish tinge but their photorefractive properties were negligible.

Since a radiation hard, Photorefractive crystal would be extremely advantageous in space applications, doping of hydrothermal sillenite crystals was attempted. Multiple dopants were tried with little improvement of the photorefractive properties. Joel Martin (OSU) and John Larkin (AFRL/SNHX) suggested trying to put excess bismuth oxide into the nutrient to obtain the bismuth on silicon defect that is apparent in the TSSG crystals. After several runs a hydrothermal BSO that was tinted yellow was grown that had photorefractive properties ("XCESS Bi" in Fig.2). The gain was 1/10th of a standard TSSG BSO sample. The crystal was radiated and showed a slight improvement of its optical properties. A sample was grown ("XCESS Bi x 2" in Fig.2) that had similar PR properties and an equivalent gain factor than that of a standard TSSG crystal but has not yet been radiated. Mg/P dopants were also tried in two runs with cast dopant, which resulted in non-uniform crystals.

Throughout the study, there has also been a problem of growth facets. When a <100> seed was used on BSO 70% of the runs resulted in growth in the <100> direction. The other 30 % of the time the growth was in some other direction or multifaceted which made for unusable crystals. The <110> and <111> seeds used had similar problems. The problem was worse with BGO and BTO, which grew predominately in a multifaceted <111> direction.

Recommendations:

Hydrothermally grown sillenites are more uniform than crystals grown from the melt. This is because of low growth temperatures, uniform growth temperature, and large fluid volume (i.e large surface growth area). Preliminary indications are that they are also radiation hardened. More work needs to be done on the radiation effects of both crystals grown from the melt and hydrothermally grown crystals. NASA and MIT are interested in the sillenites for space applications and collaborations with these groups and others should be initiated. Fig. 4 illustrates the transmission curves of various BSO crystals grown in the lab.

Uniformity, wavelength response, speed and sensitivity can be improved by continued experimentation of doping. These defects also must be understood in order to improve engineering performance of devices made from these crystals. One approach, as of yet untried, is to put an oxygen overpressure in the liners to try to get an optical defect into the crystal structure.

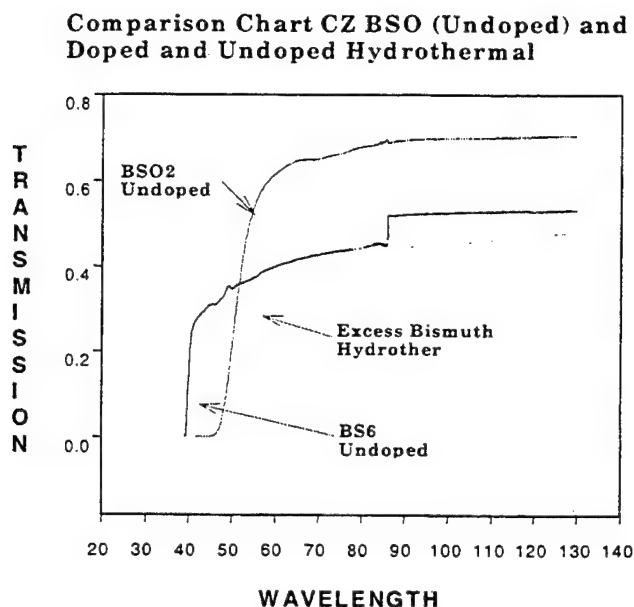


Figure 4: Transmission curve comparison of BSO

In order for the process to be scaleable, the growth interface and multifaceted growth problems must be solved. These problems could be caused by the weight of bismuth. It might be that a large kinetic energy is required in order to initiate growth on the seed. This energy causes a large amount of nutrient to dump out on the seed until a steady state solubility of bismuth oxide is reached in the growth zone. This dumping phenomenon could be one cause of the poor seed interface and multifaceted growth directions. To solve these problems the chemical dynamics of the growth mechanism need to be studied. A simulation model for hydrothermal growth of the sillenites also would be extremely helpful. Possible solutions to these two problems would be to grow in a low gravity environment or to stir the solution during growth.

Zinc Oxide Hydrothermal Growth:

Experimental :

ZnO single crystals were produced in 1" and 3" ID autoclaves. The same autoclaves used for the sillenites are used for zinc oxide (see figure 2.). Platinum liners were used to isolate the experiment from the walls of the autoclave because of the caustic nature of the solution (4 normal NaOH/KOH). Zinc oxide single crystal seeds, along with nutrients, and solvents were placed in the liner. The liner was then sealed by stick welding with platinum. The volume fill of the liner was between 70-80 percent and the proper amount of 1N NaOH solution was added on the outside of the liner to match the fill rate on the inside of the liner. The following procedures were used:

1. Nutrients preparations: 4-9s ZnO powder (Alfa Aesar) was placed, packed, pressed and sintered at 1000°C -1350°C for 2 to 24 hours in a 2 ¼ inches platinum crucible. The sintered cylinder was then crushed into ¼" to ¾" pieces.
2. Seed preparation: Hydrothermally grown ZnO single crystal seeds 0.5mm to 2mm thick were prepared with a 20 mil hole drilled through one end. Platinum wires 15 mils in diameter were placed through the hole and attached to a seed rack.

3. Mineralizer solution: was a mixture of 0.1-1m Li_2CO_3 , 3 N KOH, and 1 N NaOH, with the fill quantity at 80% (Pressure approx. 16000 psi).
4. Duration: 72 hour ramp up, run at temperature for 30-45 days, 72 hour ramp down
5. Growth Temperature: Bottom Zone- 355°C Top Zone-345°C
6. Platinum vessel 1/7th volume of autoclave 0.5 liters/3.5liters

Results and Discussion :

Thirty-eight growth experiments were performed which resulted in 45 crystals during the length of this contract. Zinc oxide has a wurtzite structure that is characterized by an anisotropy between the two surfaces on its basal plane. One surface has zinc rich, C^+ side and the other surface has an oxygen rich, C^- side. Wafers were sliced and etched in nitric acid, which identified the C^+ and C^- planes.³ Surface properties of various samples were analyzed by: double axis x-ray rocking curve with a high resolution four circle x-ray diffractometer; room temperature PL with a 0.25m grating monochromator, ccd detector, and a 275nm, 5ns pulsed variable wavelength laser source. Hall, Mass Spectrometer, AFM, and Sims measurements were also done on various samples.

The first series of runs (ZnO 1-17) resulted in poor quality crystals with inclusions. The gradients were refined and higher quality seeds were used. This resulted in crystals with less inclusion and optical quality samples up to 1cm square were obtained. It was discovered that growth rates in both directions on the basal seed plates averaged 10 mils per day for the 30 day runs, but growth was typically anisotropic: the ratio of growth rates between the fast (C^+) and slow (C^-) growth directions was 3 to 1. This 3 to 1 growth was not consistent for all runs. Some runs had nearly even growth on both sides of the basal plane while other runs the C^+ side had up to 5 times the growth rate of the C^- side. The C^- side was typically a dark greenish color whereas the C^+ side was clear or slightly yellow.

In the photo below are two polished samples 1.5mm thick from the C^- and the C^+ sides of ZNO 37. The samples have narrow rocking curves (less than 50 arcseconds), pronounced room temperature PL, and transmission curves that are characteristic of high quality material.



Figure 5: ZNO 37 C^- and C^+ faces

A collaboration was made with AFRL/MLPO and it was determined that surface preparation is a critical factor in producing a high quality ZnO surface. The surface preparation was also verified by an improvement of low temperature PL done at MLPO. Eagle Picher has a proprietary polishing method for zinc oxide, which was done on one of the zinc oxide samples

grown at Hanscom. The table below shows a substantial improvement of surface quality is achieved when the proper polish is applied.

<i>Surface Preparation Description</i>	Mechanical polish		Eagle Picher polish	
Crystal faces	C ⁺	C ⁻	C ⁺	C ⁻
X-ray rocking curve FWHM (arc-sec)	108	104	43	37
3.28 eV PL relative intensity at room temp	0.04	0.5	1.1	1.5

Table III: Effect of different surface treatments on hydrothermal ZnO

A dopant study was done on a series of samples. Preliminary indications are that impurities get incorporated differently in the various growth directions of the crystal. There are also indications that all areas are oxygen deficient to varying degrees. The dark areas seemed to have more impurities, lower resistivity and a higher free carrier concentration than the light areas from the Hall measurements that were taken. There are still some ambiguities in these measurements that need to be addressed. A few experiments were done to reduce the oxygen defects by adding hydrogen peroxide to the solution.⁴

Recommendations:

An in-depth study should be done on the effects that temperature, pressure, gradient, solute, distance between seed and nutrient, and baffle geometry have on growth rates and crystal quality. A platinum-lined autoclave was recently optimized for zinc oxide growth for this purpose. For a semiconductor, the purity of the substrate plays a critical role in device performance. Hydrothermal zinc oxide substrate impurities need to be reduced. This can be done by using high purity solvents and nutrients and by post treating of the crystals.

Research should be done on the addition of dopants to change the properties of ZnO to tailor it for specific applications. Hydrothermally grown crystals are zinc rich. Oxygen could be incorporated into the crystal by addition of an oxygen overpressure in the solvent by the addition of hydrogen peroxide, or other oxygenating solvent. Analysis and further adjustment of the parameters of hydrothermal growth would produce crystals that are close to intrinsic and are highly insulating. Acceptor impurities could perhaps be incorporated in a low temperature, high surface area regime like hydrothermal growth. A P-type zinc oxide substrate will open a whole new area of device applications.

Surface properties of zinc oxide also need to be studied. Zinc oxide is a soft material and can be easily damaged. In order for zinc oxide to be a viable material surface damage must be controlled. The C⁻ and the C⁺ sides of the substrate are affected differently by various surface preparation techniques. Optimal preparation techniques need to be developed.

Nitride ammonothermal growth:

Experimental:

Loading, operation, and unloading of ammonia solutions in nickel based autoclaves was done in a specially made containment room. The containment room contained a loading system

in a lab hood, two chambers for running the experiments, and all the required control systems for reliable and safe operation of high pressure ammonia autoclaves. The two type Rene 41 autoclaves used have an inner chamber 14" long with a volume of 140 cc and are capable of temperatures up to 600 degrees Celsius and a pressure of up to 60,000 pounds psi. The autoclaves were loaded in a glove box containing nitrogen with less than 3 ppm oxygen and water vapor. Sodium amide or potassium, and 99.9% pure GaN powder or 99% pure polycrystalline AlN were loaded into a nickel container that had a baffle and seed rack attached.

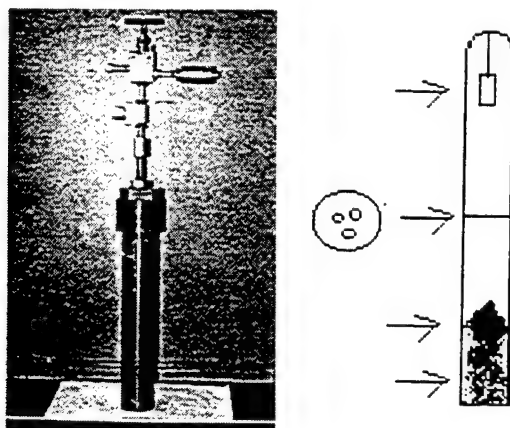
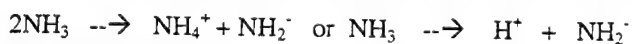


Figure 6: Picture of Autoclave and nickel liner assembly

Sapphire or other seeds were prepared and attached to the seed rack 2-4 inches above the GaN or AlN nutrient. The Baffle system was then inserted into the autoclave and the bolt fitting, sealing nut were tightened down. The autoclave was then removed from the glove box and the sealing nut was torqued down with a six foot long sealing bar. The autoclave was then weighed on a 50 kilogram scale and installed in the ammonia transport system in the containment room and filled with ammonia until 60-80% fill was reached. Thermocouples were then attached and the autoclave was inserted into a box furnace. The autoclave was then heated at 200- 400°C for 7-21 days. Upon completion of the run the autoclave was inserted into the ammonia loading system to remove the ammonia. The autoclave was then loaded into the glove box and the baffle system was removed for inspection. The autoclave was then cleaned thoroughly and readied for the next experiment.

Results and Discussion:

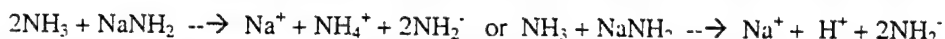
Ammonothermal growth is the corollary of hydrothermal growth in which ammonia is used as a solvent instead of water as shown in the equation below.



Equation 1: Pure ammonia solution

In pure ammonia the ion product is much smaller than water at 10^{-33} . The small amount of ions in pure ammonia allows the alkali metals to be dissolved directly in ammonia without causing the violent reactions typical of dissolving alkali metals in water. The alkali metals decompose in ammonia to hydrogen and the corresponding metal amide. The decomposition is very low for lithium and sodium and increases for the heavier alkali metals in which cesium is

completely converted to cesium amide⁵. The alkali metal amides can now be used to make the ammonia solution basic as the alkali hydroxides are used to produce more ions in water.



Equation 2: Ammonia base solution.

If the solubility of GaN, AlN, or InN (nitrides) is sufficient in the basic ammonia solution the nitrides should dissolve. If the solubility changes with temperature, then an increase or decrease in temperature, depending if the nitrides have a negative or positive solubility, would cause the nitrides to come back out of solution. If this process is controlled then single crystals can be produced.

The nitrides were dissolved in the first series of runs but did not come out of solution. Instead an amide complex was formed with the metal (Ga or Al) and the alkali metal. This is similar to water glass being formed in hydrothermal quartz growth instead of quartz. A salt (potassium bromide) was added to the last experiment performed to avoid the amide complex. Indications were that small GaN crystals had formed on this run, but crystalline nutrient was used. To be sure that the GaN was crystallized out of solution the experiment needs to be repeated. The table below summarizes the results.

Run Name	Days run	Solute used	Seed Etched	Hydrogen Pressure End of Run	Presence of metal Amide after run	GaN crystallized out of solution
GaN1	14	0.5 g NaNH ₂	No	No	No	No
AlN1	14	0.5 g NaNH ₂	No	No	No	No
GaN2	21	4.5g K	Yes	Yes	Yes	No
AlN2	21	3.5g K	Yes	Yes	Unknown	No
GaN3	15	3g K 2g NaBr	Yes	Yes	Unknown	Up to 0.1mm ?

Table 3: Results of AFRL ammonia thermal experiments

Recommendations:

Work needs to be done at AFRL at Hanscom in redesigning the system and developing correct parameters to establish conditions that enable crystallization of GaN polycrystalline and single crystals by the ammonothermal method. Research should be conducted to investigate the effect of the following parameters on the growth cycle of GaN, AlN, and InN.

- 1) Addition of a catalyst such as iron has increased the rate and amount of ionization of various amides. Various catalysts should be attempted to increase the solubility of the amides
- 2) The ionization can also be increased by combining the alkali amides and by using cesium or rubidium amide
- 3) Addition of halide-metal (Al, Ga, In halides) compounds in amide/ammonia solutions has shown promise of producing Al, Ga, and In amides. Small crystals of gallium and aluminum nitride were produced both here and at Clemson University⁶ using these salts in basic ammonia solution. A complete study of these salts in basic ammonia solution should be accomplished.
- 4) Several experiments converted Al and Ga metal to the corresponding nitrides in amide/ammonia solutions. These resulted in less than 1mm size crystallites.

- 5) Amide/ammonia solution is one of the most conductive electrolytic solutions and growth might be able to be stimulated by inducing a current in the solution.
- 6) A slow temperature ramp could also stimulate growth.

All these parameters should be theoretically and experimentally tested. A unit similar to a Barnes Volumetric Hydrothermal system should be developed for solubility and kinetic studies. Once GaN and AlN growth can be established, the process should then be evaluated for traditional parameters such as temperature gradient, pressure, and baffle design in order to establish optimal operating conditions for growth of gallium nitride and aluminum nitride bulk crystals. At this point doping of the bulk crystal to tailor the resistance of the material should be attempted.

Nitride vapor phase growth:

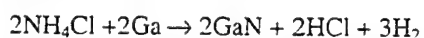
Experimental:

Chemical vapor transport of crystals involves using a transport agent to promote a chemical reaction in order to produce the required substance. Early attempts of growing nitrides were based on using ammonia gas as a transport agent. The reaction involved flowing ammonia over gallium to produce gallium chloride and depositing GaN on a substrate by chemical reaction of the gallium chloride and ammonia⁷.



Equation 3: CVD of GaN

Several variations of the reactant gas have been attempted such as GaCl₂, GaCl₃, and others. AFRL has found that ammonia chloride (NH₄Cl) is a promising transport agent for chemical vapor transport of the nitrides. The chemical reaction is shown below.



Equation 4: CVD of Ammonia Chloride of GaN

Chemical vapor transport experiments were conducted in silica-based ampoules using ammonia chloride as the transport mechanism. The chemical reaction is shown below.



Equation 5: CVD of GaN using Ammonia Chloride and nitride

Originally GaN nutrient was used and did not produce any noticeable transport thus gallium and aluminum metal was used.



Equation 6: CVD of GaN, AlN, or InN using Ammonia Chloride and metal

The nutrients, seeds, and ammonia chloride were loaded in silica ampoules in a nitrogen glove box. The ampoules were either sealed under vacuum after purging in nitrogen or a quasi open system with a balloon attached on end was used. The ampoule was then placed in a furnace and insulation was placed at each end of the ampoule. Growth temperature ranges were from 600⁰ to 1050⁰ Celsius. Growth time was from 1 days to 38 days. In the closed ampoule, less than a gram of material could be produced because the HCl and H₂ byproducts introduced a large amount of gas and therefore pressure. The quasi-open system contained 1-10 grams of material. Growth time ranged from 2 to 8 hours. The vapor transport agent in both systems was ammonia chloride. A picture of the ampoule is shown in Fig 7.



Figure 7: Quasi open vapor phase system

Three open systems with flow controllers were also constructed. These systems ran 95% N_2 / 5% H_2 over ammonia chloride that was heated to 200-300°C. The forming gas then flowed over molten gallium at 700-1050°C. A diagram of this system is shown below.

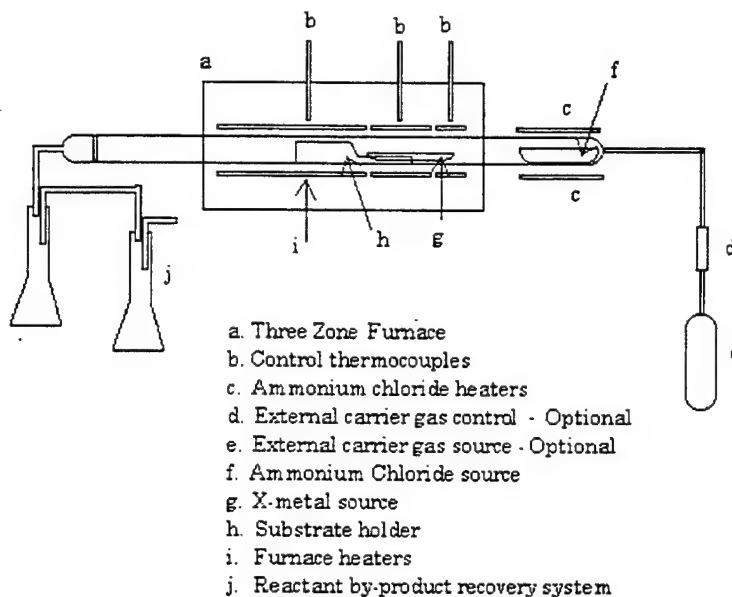


Figure 8: Open vapor growth system of nitrides

Results and Discussion:

There were 40 GaN, 8 AlN, and 3 InN closed and quasi experiments performed. Initially the growth of the closed and quasi systems produced only powder or submillimeter sized crystals. AlN, SiC and zinc oxide seeds were used in the various runs. SiC appeared to have the best nucleation and some small hexagonal nitride crystals were found on them. Any oxygen would contaminate the experiments, so zinc oxide was not a good seed candidate. It was discovered that aluminum was oxidized too easily, and growth was restricted because of the oxide layer that formed on the surface. This was overcome by etching aluminum in gallium in the glove box during the loading of the ampoules. Growth of alloys of different metals was also attempted with some indication of crystalline structure.

Ammonia bromide was used as a transport agent instead of ammonia chloride. Growth was slower with the ammonia bromide with the same parameters used. A combination of ammonia bromide and ammonia chloride produced the best results in the closed and quasi systems.

The open systems produced hundreds of GaN plate from 0.1-7mm long by 0.1-3mm wide by 10-100 microns thick. One of those plates is pictured in Fig 9.

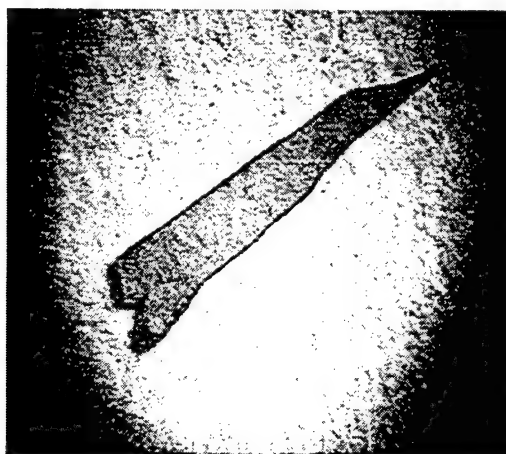


Figure 9: Gallium Nitride single crystal plate

These plates have pronounced PL, and rocking curves under 100 arc seconds. The plates were from clear to black, which indicates a range of intrinsic to gallium rich crystals.

Recommendations :

This research could be continued to modify the system to produce single crystal nitrides at high growth rates by investigating the following:

- 1.) Ampoules design - shape, material, and placement of seeds and nutrients holding devices.
- 2.) A new reactor design with individual temperature heaters and controls for seeds, nutrient, and ammonia chloride for the quasi system.
- 3.) Investigate other seeds as substrate materials.
- 4.) Conversion of the open system in which the use of other carrier gas such as ammonia can be introduced to help reduce the gallium overpressure. Explore additional nitrides and alloys.
- 5.) Have a controllable source for gallium, such as GaCl or use of an atomizer for the gallium.
- 6.) Attempt to use GaN, InN, and AlN instead of Ga, In, Al at higher temperature in an effort to increase the amount of monatomic nitrogen at the growth interface.

References

1. B. Horwitz and F. Corbett, Opt. Eng. **17**, 353 (1978)
2. M. T. Harris, J. J. Larkin, and J. J. Martin, Appl. Phys. Lett. **60**, 848 (1992).
3. A. N. Mariano and R. E. Hanneman, J. Appl. Phys. **34**, 384(1963).
4. Noboru Sakagami, J. of Crystal Growth **99**, 905(1990).
5. Non-Aqueous Solvents, Audrieth and Kleinberg, John Wiley & Sons, NY (1953) 95.
6. Joseoh W. Kolis, et al., Mat. Res. Soc. Symp. Proc. **495**, 367(1998).
7. H. P. Maruska and J. J. Tietjen, Appl. Phys. Lett. **15**, 327 (1969).

TECHNICAL ACTIVITY:**Introduction:**

Silicon is the prevalent semiconductor material at the present time, accounting for over 90% of the total devices used for commercial and military applications. It is limited for optical applications because of its indirect bandgap. GaAs is a direct bandgap material and can be run at higher power and speeds than silicon. However, the Air Force has many device requirements for future systems that currently cannot be fulfilled with present semiconductor materials such as Silicon or GaAs. Solid State Scientific Corporation (SSSC), and myself in particular, have been working with AFRL/SHNX for four years in research and development in the melt growth in high pressure (>30 atm.) of indium phosphide bulk crystals. Indium phosphide devices are used for high speed high power devices, outperforming GaAs devices (InP HEMPT- 600 GHz f_{max} , 16.1 dB gain at 94 GHz (Sanders Microelectronic Facility). Since indium phosphide has a direct bandgap at 1.15 eV it is also perfectly suited for fiber optical communication devices. A diagram (Fig. 1) shows how indium phosphide stacks up against other alloys and its importance as a III-V semiconductor compound. Indium phosphide devices are expensive because of the cost of InP substrates. Bridgman growth is the most common method of growth, but is capable of only three-inch wafers compared to six-inch GaAs wafers. Czochralski growth is also done but in a two-step injection/growth process which is cost and time consuming. SSSC has been supporting AFRL/SHNX in growing indium phosphide substrates by in-situ Magnetic Liquid Encapsulated Kyropulos (MLEK) to develop a cost effective method of producing four-inch and larger InP substrates. Devices such as field effect transistors and high speed photoconductive switches depend on these uniformly doped crystals with very low residual impurity concentrations and dislocation densities.

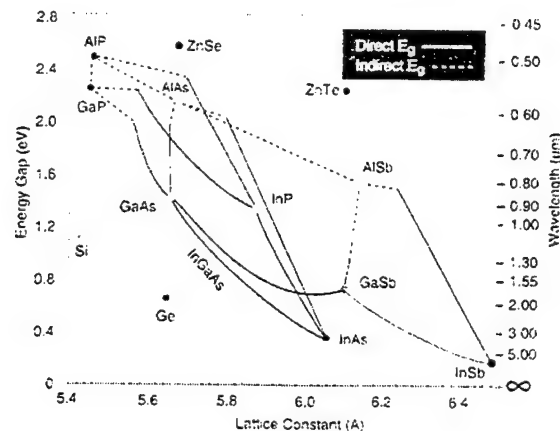


Figure 1. Bandgap and lattice structure of various semiconductor materials.

First Generation Puller:

Over a three year period, nearly 120 growth experiments using a puller depicted in Fig. 2 have been performed. The chamber is RF heated and water cooled. The crucible containing the indium can be heated to 1200°C and the furnace has an over-pressure of 600 psi of either argon or nitrogen. A 4k gauss magnet is employed to stabilize the melt growth. The chamber has an injector for the phosphorous that is heated from the melt below. The injector can be swung to one

side to allow a seed rod to be lowered into the melt. A typical run would begin with the melting of the indium and then encapsulating it with B_2O_3 (glass). Next the injector tube is lowered into the melt, which increases the temperature of the phosphorous from the radiant heat of the melt. The heated phosphorous becomes a gas which is injected into the indium melt. The phosphorous then reacts with the indium melt and forms indium phosphide.

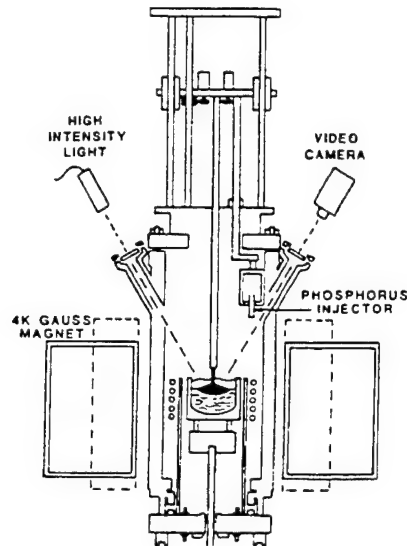


Figure 2. The InP MLEK Puller

The B_2O_3 prevents the phosphorous from escaping from the indium due to the higher vapor pressure. Finally the injector is removed and a single crystal seed is lowered into the InP melt through the B_2O_3 , which is viscous. Using a technique developed here at Hanscom, a magnetic field is applied which helps stabilize the melt to grow a Kyropoulos style (flat top face) rather than the industry standard cone top ingot. This minimizes wasted material when the ingot is sent out and sliced into wafers. At any point, if twinning is observed the crystal can be re-melted and started again. The crystal is pulled up at 0.3-1.0cm per hour with the entire process lasting 7-10 hours. Results of a successful run are shown in Fig. 3. These crystals form the basis for fabricating wafers used in creating optoelectronics and radio frequency electronics.

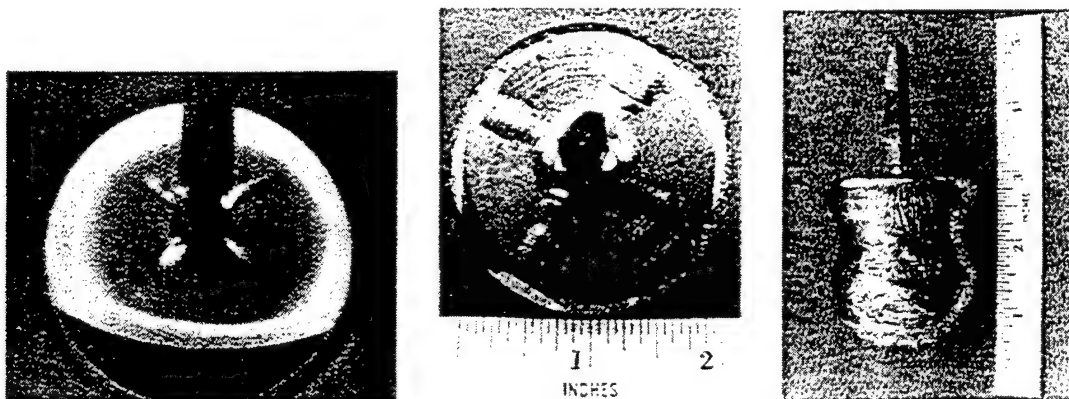


Figure 3. InP MLEK grown single crystal ingots.

In a unique transfer of technology, AFRL/SNHX has been very instrumental in sharing these wafers with both industry and academia. Many papers and conferences have been given on results emulating from these experiments. The two most recent papers deal with a series of runs which studied first, controlling the seeding technique to suppress the propagation of dislocations (twins) from the seed/melt interface and second, the use of a cusped magnetic field during bulk growth. The first paper's experiments demonstrated that most of the dislocations are screw dislocations emerging from the seed-crystal interface (see Fig. 4). Since these dislocations propagate along $\langle 111 \rangle$ planes, it is possible under certain geometric conditions, to allow the dislocations to grow out of the $\langle 100 \rangle$ crystal by adopting a necking procedure.

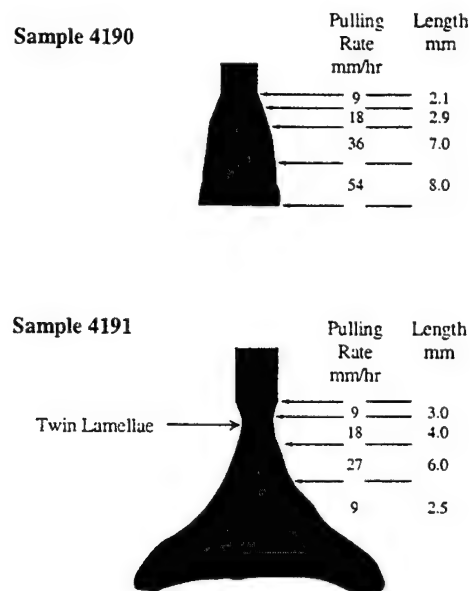


Figure 4. Cross section of two InP crystals used in the seed/necking experiment.

The necking procedure is a very effective strategy for obtaining dislocation-free InP throughout a relatively small diameter. Our research raises the possibility of growing large diameter, highly perfect InP single crystals. To be able to control the seeding at the start of a run would go a long way in keeping dislocations from propagating through the crystal. The second paper dealt with the investigation of crystal growth under two different magnetic field configurations (Fig. 5). Axial field growth enhances melt stability, but increases the radial thermal gradient. This configuration contributes to crystal growth control and reduces twin formation. The axial field strength is strongest in the center of the growth chamber, where the crucible is located. On the other hand, for a cusped configuration, the radial component of the field is stronger than the axial component in the mid-section. However, because of the large inside diameter of the magnet coils required for the thick wall high-pressure growth chamber, the cusped field proved too weak to stabilize the melt. Crystals grown in the cusp configuration resemble those grown without any applied field. The melt-solid interface shape is convex for both configurations, but slightly flatter for growth in a cusped field. Given the small effect of this field configuration, there was no observable improvement in crystal growth resulting from the application of a cusped magnetic field.

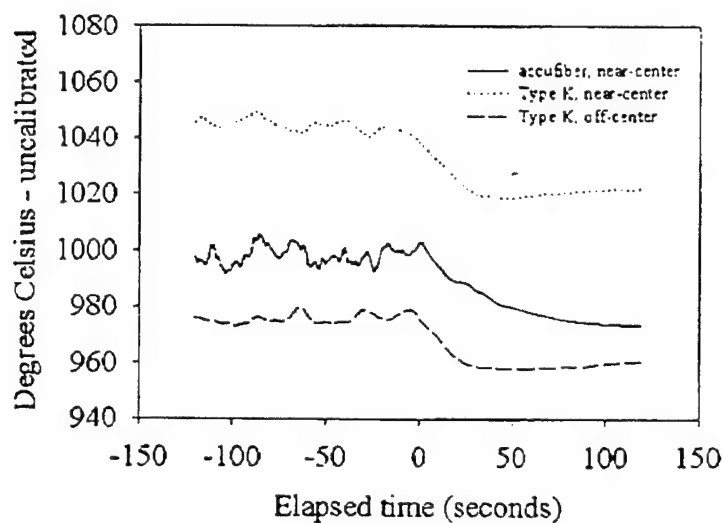


Figure 5a. Off and on of axial magnet transition at 12mm from bottom.

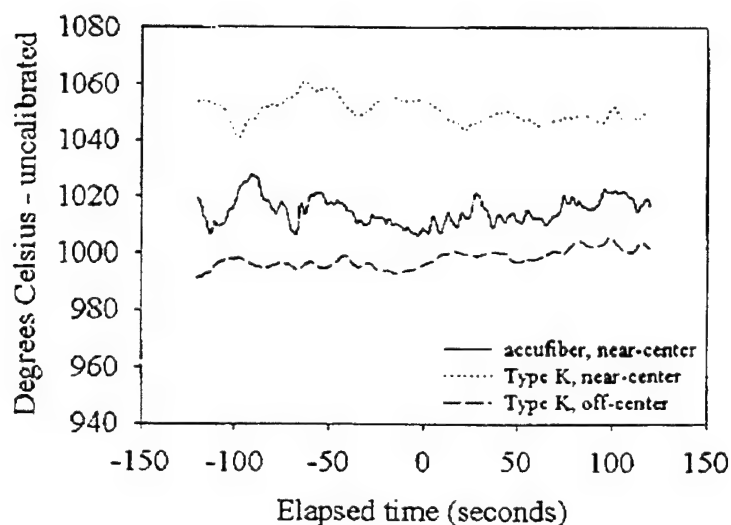
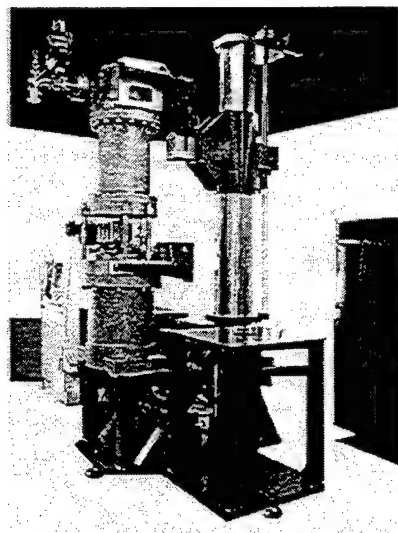


Figure 5b. Off and on of cusped magnet transition at 12mm from bottom.

Next Generation Puller:

To make our technology growth more efficient and reproducible, the Sensors Directorate collaborated with State University of New York (SUNY) Stonybrook's Center for Crystal Growth under the Air Force Office of Special Research (AFOSR) sponsored Summer Faculty Research Program. A subsequent meeting of the AFOSR Working Group on High-Pressure Crystal Growth at Hanscom AFB in the summer of 1993 contributed to the definition of a Multidisciplinary University Research Initiative (MURI) topic on crystal growth. Professor Vish Prasad at SUNY Stonybrook later organized several research groups for a MURI proposal, which resulted in AFOSR and Defense Advanced Research Prospects Agency (DARPA) sponsorship of an integrated intelligent modeling, design and control program of the crystal



Features:
 High Pressure Stainless Steel
 Upper Chamber for synthesis
 Lower Chamber for growth
 Magnetic field stabilization
 Resistance heated injector
 Load cell controls for:
 Synthesis stoichiometry
 Crystal diameter 4-6 inch

Figure 6. GTI model 100 high pressure III-V semiconductor crystal growth system.

growth process. January 1999 was the beginning of the dual-use program involving AFRL/SNHX, Stonybrook University, GTI Equipment Technologies Inc. of Nashua, NH, and MA/COM (Lowell). The new Model 100 High Pressure III-V Semiconductor Crystal Growth System (Fig. 6) has been delivered and is capable of making up to six-inch InP single crystal ingots by the one-step in-situ synthesis process. SUNY Stonybrook was responsible for the simulation codes which optimize the crystal growth parameters in the new system along with code inputs for boundary conditions and physical properties established by experiments done in-house at Hanscom. The primary function of this new puller will be to grow bulk semiconductor InP crystals for fiber optic communications, advanced terrestrial and space based communications, advanced military radar, and emerging civilian radar applications such as automotive collision avoidance systems. By combining the two functions of synthesis and growth into one system, wafer manufacturers will be able to now produce affordable, high quality InP wafers for many applications.

Future Work:

The long range goal is to grow high quality InP single crystals for both the Air Force and the private sector. A series of injection only runs has begun which will gather enough data so design modifications can be made to optimize the system. When the two year dual-use program is completed, a production furnace design will be forthcoming for GTI to sell a HP furnace that will yield not only high quality six-inch InP wafers, but also other III-V compounds such as GaAs, ZnGeP₂, CdGeAs₂, and GaP. My duties will continue to provide support and expertise in all facets of this effort to obtain the highest level of growth possible, improve the stoichiometry of the crystals and the controlling and stabilization of the melt gradient.

TECHNICAL ACTIVITY:

My activity has been research, design and implementation of mathematical algorithms for optimizing numerical procedures in varying reconstruction algorithms for the angularly multiplexed spectral imager, designed and fabricated at AFRL, Hanscom AFB by J. Mooney, et. al. [1]

1. Introduction:

The spectral imager, under this project, collects a sequence of chromatically dispersed images over all the spectral bands and then computationally reconstructs the chromatic information. Chromatic dispersion is obtained by a pair of rotating prisms, and collected data is arranged in a three-dimensional cube. An image displacement is modeled as a convolution with a displaced delta function, and recorded data at spatial position (x,y) , at prism angular position ϕ_m , is represented as

$$r(x,y,\phi_m) = \sum_k p_{m,k}(x,y) ** c(x,y,k),$$

where $c(x,y,k)$ is the desired spatial-chromatic object information and

$$p_{m,k}(x,y) = \delta(x-(k-k_0)) \Delta x \cos(\phi_m), y-(k-k_0) \Delta x \sin(\phi_m),$$

with the pixel dimension Δx on the focal plane array and k_0 is the undeviated spectrum given by the rotation axis of the prisms. $c(x,y,k)$ is solved computationally by a matrix inversion in the Fourier domain. Applying the two-dimensional, spatial Fourier transform to both sides, we have

$$R(\xi,\zeta,\phi_m) = \sum_k P_{m,k}(\xi,\zeta) C(\xi,\zeta,k),$$

where (ξ,ζ) is the spatial frequency variable. For each spatial frequency variable, we have a matrix equation of size $M \times K$,

$$[R(\xi,\zeta)]_{0 \leq m < M} = [P(\xi,\zeta)]_{m,k} [C(\xi,\zeta)]_{0 \leq k < K},$$

where M is the number of distinct prism orientation and K is the number of discrete, sampled chromatic bands. The reconstruction algorithm is a two-step procedure of directly inverting the matrix for each sampled, spatial frequency and an iterative procedure of enhancement. For each ϕ_m , $r(x,y, \phi_m)$ is recorded on a $N \times N$ focal plane array, and determines the spatial sampling.

Computational requirements for the matrix formulation of the problem is collection of M two-dimensional, $N \times N$ forward, and K inverse Fourier transforms. A reconstruction is obtained by $N^2 M \times K$ matrix inversion. Varying algorithms for enhancement have been implemented. Computational requirements and bottlenecks are different in each of the algorithms, but spatial filtering, singular value decomposition and matrix operations will be discussed in this report.

2. Mixed And Higher Radix Fourier Transform Algorithms:

Implementation of the fast Fourier transform (FFT) kernels are based on the algorithms in [2,3]. Choice of varying parameters in the algorithms have been based on the specific nature of the problem and sizes, and the machine parameters. A collection of routines implementing two-dimensional, origin shifting FFT algorithms for real data has been implemented. As compared to existing FFT routines based on [4], these routines run 4-8 times faster.

2.1 Two-Dimensional Powers Of Two FFT:

A collection of optimized 2-dimensional powers of two FFT algorithms have been implemented. The optimization is based on higher order, mixed radix Cooley-Tukey algorithm matching the register size of a SUN system and the Pentium processor. This implementation is also tailored to match the input/output data structures surrounding FFT computations. The algorithms are based on radix 4/8-Cooley-Tukey FFT. Every power of 2 can be expressed as a product of a power of 4 and a power of 8. This expression however, is not unique, leading to ambiguity in algorithm design. For example,

$$2^6 = 64 = 8^2 = 4^3.$$

Maximal use of the register capability of the Pentium processor calls for radix-8, while data transfer uniformity calls for even decomposition of the size. For example,

$$2^9 = 512 = 8^3 = 32 \times 16 = (8 \times 4) \times (4 \times 4),$$

512-point FFT can be implemented by 3 iterations of radix 8 or radix 8 followed by 3 iterations of radix 4. Optimal implementation thus varies from processor to processor, depending on the architecture. Incorporating these parameters, sizes ranging from 2-dimensional 32 to 1024 have been implemented. These routines also incorporate origin shifting.

2.2 Two-Dimensional Mixed Size FFT:

A collection of optimized 2-dimensional mixed size FFT algorithms have been implemented. The optimization is based on higher order, mixed radix Cooley-Tukey and Good-Thomas algorithms. This collection includes sizes that are multiples of 15. The algorithm is based on the Chinese remainder theorem for the indexing ring \mathbf{Z}/N , the integers module N , for $N=480$. For $N = KL$, where K and L are relatively prime, the Chinese remainder theorem implies that

$$\mathbf{Z}/N \approx \mathbf{Z}/K \times \mathbf{Z}/L.$$

The isomorphism and its inverse are given by the system of idempotents, $\{e_1, e_2\}$, defined by

$$\begin{aligned} e_1 &\equiv 1 \text{ mod } K, & e_1 &\equiv 0 \text{ mod } L, \\ e_2 &\equiv 0 \text{ mod } K, & e_2 &\equiv 1 \text{ mod } L. \end{aligned}$$

e_1 and e_2 satisfy

$$e_1^2 \equiv e_1 \text{ mod } N, \quad e_2^2 \equiv e_2 \text{ mod } N,$$

$$e_1 e_2 = 0, \quad e_1 + e_2 = 1.$$

The isomorphism is given by

$$n \rightarrow (n_1 \bmod K, n_2 \bmod L), \quad n \in \mathbf{Z}/N, n_1 \in \mathbf{Z}/K, n_2 \in \mathbf{Z}/L,$$

with the inverse

$$(n_1, n_2) \rightarrow e_1 n_1 + e_2 n_2 \in \mathbf{Z}/N.$$

Indexing the input of the Fourier transform by the inverse isomorphism and the output by

$$(n_1, n_2) \rightarrow K n_1 + L n_2 \in \mathbf{Z}/N,$$

respectively, we have that

$$F(N) = F(K) \otimes F(L),$$

where $F(N)$ denotes the N -point transform and \otimes denotes the tensor product of linear transforms.

A good deal of this theory is well documented in literature and often called the Good-Thomas prime factor algorithm, but the output indexing scheme is new. As compared to more commonly used Cooley-Tukey FFT, Good-Thomas PFA is more efficient in terms of complexity, but less advantageous in the data flow. Optimization of the algorithm is thus solely dependent on controlling the input and output of the data flow. This optimization has been carried out for 2-dimensional FFT routines, using 15-point and powers of two optimized kernels.

2.3 1-Dimensional Prime Size FFT:

A collection of optimized 1-dimensional FFT algorithms have been implemented for spatial filtering operations. These routines hybrid Good-Thomas prime factor algorithm and field algorithm for prime size kernels of up to prime factor 29. The prime p size kernels are implemented using Rader's field algorithm to reorder the input/output to rewrite the prime point Fourier transform matrix as a skew-circulant matrix of dimension $p-1$, then diagonalizing by the $p-1$ point Fourier transform matrix.

2.4 FFT Of Real Data Sequences:

An algorithm to address real valued input data characteristic is also designed. Since this algorithm is not very well documented in literature, it is described here. The N -point Fourier transform is given by

$$f(y) = \sum f(x) \exp(-2 \pi j/N),$$

where $i = (-1)^{1/2}$. For real valued data $f(x)$, we have that

$$f^*(y) = [\sum f(x) \exp(-2 \pi i/N)]^*$$

$$\begin{aligned}
&= \sum f^*(x) \exp(2 \pi i/N) \\
&= \sum f(x) \exp(2 \pi i/N), \\
&= f(N-y),
\end{aligned}$$

where * denotes the complex conjugate.

Thus the output of the Fourier transform of real data is Hermitian symmetric, requiring only half of the output as the essential information. The formulation and algorithm is given below for two sequences for simplicity, but extension to many sequences is immediate.

Let $f(x)$ and $g(x)$ be two sets of N real data. Define two new sequences $h(x)$ and $k(x)$ by

$$h(x) = f(x) + ig(x), \quad k(x) = f(x) - ig(x).$$

Then

$$f(x) = 1/2(h(x) + k(x)), \quad g(x) = -i/2(h(x) - k(x)).$$

Since FT is linear, we can compute the FT of f and g by computing the FT of h and k . Notice now that $k = h^*$. Thus the FT of h is given by the time reversal of complex conjugate FT of k . Using this fact, the FT of f and g can be computed by computing the FT of h only.

$$f^\wedge(y) = 1/2(h^\wedge(y) + h^{\wedge*}(N-y)), \quad g^\wedge(y) = -i/2(h^\wedge(y) - h^{\wedge*}(N-y)).$$

Algorithm overhead is the interleaving of the two real sequences of data, and the arithmetic required (additions only) in extracting the result.

3. System Transfer Matrix:

The first step, direct inversion procedure in the reconstruction algorithm, is a localized (block diagonalized) pseudo-inverse matrix computation. A pseudo-inverse of a matrix can be computed by the singular valued decomposition (SVD). For a $K \times M$ matrix H , SVD computes three matrices, unitary matrices U and V of sizes $K \times M$ and $K \times K$, respectively, and a diagonal matrix Σ of size $K \times K$ such that

$$P(\xi, \zeta) = U \Sigma V^+,$$

where V^+ is the transpose-conjugate of V . Since U and V^+ are unitary, we have

$$V^+ V = U U^+ = I_K$$

where I_K is the $K \times K$ identity matrix. The diagonal entries of Σ are taken as non-negative real numbers, and can be ordered in descending order,

$$\Sigma(0,0) \geq \Sigma(1,1) \geq \dots \Sigma(l,l)$$

$$\Sigma(l+1,l+1) = \Sigma(l+2,l+2) = \dots = 0.$$

Set

$$\Sigma'(k,k) = 1/\Sigma(k,k), \quad \text{for } 0 \leq k \leq l,$$

$$\Sigma'(k,k) = 0, \quad \text{for } k \geq l.$$

Then

$$V \Sigma' U^+ = \text{Diag} (1, 1, \dots, 0, 0, 0)$$

and $H' = V \Sigma' U^+$ is the pseudo-inverse of H .

For each of the spatial-frequency variable (ξ, ζ) , computation of $P(\xi, \zeta)$ is sufficient for the direct inverse step of the algorithm. However, the decomposition $U(\xi, \zeta)$, $V(\xi, \zeta)$ and $\Sigma(\xi, \zeta)$ are stored for use in varying iterative algorithms. Although pseudo-inverse matrices are precomputed, significant processing time is spent accessing large amounts of data required in storing the processed results.

Extensive research has been carried out to exploit the symmetries and periodicities in the system transfer matrices $P(\xi, \zeta)$ to reduce storage and computational requirements. This has resulted in elimination of disc accessing, speeding up the overall procedure by many fold.

Let K, M and N be natural numbers, and \mathbf{N} a collection of consecutive integers of order N . For $-M/2 \leq m < M/2$, $n \in \mathbf{N}$, set $\phi_m = 2\pi n/M$ and define

$$h_{m,n}(x,y) = \delta_{n \cos \phi_m, n \sin \phi_m}(x,y), \quad (x,y) \in \mathcal{H} \times \mathcal{H}.$$

Denote by \mathcal{Q} the set

$$N/K\mathbf{Z} \times N/K\mathbf{Z} = \{ (k, l) : (k, l) \in \mathbf{Z} \times \mathbf{Z}, -K/2 \leq k, l < K/2 \}.$$

Throughout the rest of this discussion, we will identify the elements of \mathcal{Q} with (k, l) . Let \mathbf{U} be the union of the support of $h_{m,n}$, $M/2 \leq m < M/2$, $n \in \mathbf{N}$ and define the map L from \mathbf{U} into \mathcal{Q} by the following rule: $L(x, y) = (k, l) \in \mathcal{Q}$, where $k \leq x < k+1$ and $l \leq y < l+1$. Let $L(n \cos \phi_m, n \sin \phi_m) = (k, l) \in \mathcal{Q}$. Define

$$g_{m,n} = w_{-}(m,n) \delta_{nk,l} + w_{+} \delta_{k+l,k} + w_{-}(m,n) \delta_{k,l+l} + w_{++} \delta_{k+l,l+l},$$

where

$$w_{-}(m,n) = (k+l-n \cos \phi_m)(l+1 - n \sin \phi_m),$$

$$w_{+}(m,n) = -(k-n \cos \phi_m)(l+1 - n \sin \phi_m),$$

$$w_{-+}(m,n) = -(k+1-n \cos \phi_m)(l-n \sin \phi_m),$$

$$w_{++}(m,n) = (k-n \cos \phi_m)(l-n \sin \phi_m).$$

For $(\xi, \zeta) \in \Omega$ we have the Fourier transform $G_{m,n}$ of $g_{m,n}$,

$$G_{m,n}(\xi, \zeta) = w_{-}(m,n) \exp(-2 \pi i/K (\xi + \zeta))$$

$$+ w_{+}(m,n) \exp(-2 \pi i/K (\xi(k+1) + \zeta l))$$

$$+ w_{-+}(m,n) \exp(-2 \pi i/K (\xi k + \zeta(l+1)))$$

$$+ w_{++}(m,n) \exp(-2 \pi i/K (\xi(k+1) + \zeta(l+1)))$$

Set

$$W(m,n, \xi, \zeta) = w_{-}(m,n) + w_{+}(m,n) e(-2 \pi i/K \xi)$$

$$+ w_{-+}(m,n) e(-2 \pi i/K \zeta) + w_{++}(m,n) e(-2 \pi i/K (\xi + \zeta)).$$

Since

$$W(m+M/2, n, \xi, \zeta) = W^*(m,n, \xi, \zeta), \quad G_{m,n}(\xi, \zeta) = G_{m+M/2,n}^*(\xi, \zeta).$$

Thus the $M \times N$ matrix of G for a given (ξ, ζ) is of the following form.

$$[G(\xi, \zeta)] = [A \setminus A^*].$$

$$[G^*(\xi, \zeta)]^t [G(\xi, \zeta)] = [A^{*t} A^t] [A \setminus A^*] = A^{*t} A + A^t A^*$$

$$= A^{*t} A + (A^{*t} A)^* = 2 \operatorname{Real}(A^{*t} A) = 2(A_1^t A_1 + A_2^t A_2),$$

where

$$A = A_1 + iA_2, \quad A_1, A_2 \in \mathcal{H}.$$

Note

$$A^{*t} A = (A_1 + iA_2)^{*t} (A_1 + iA_2) = (A_1^t - iA_2^t)(A_1 + A_2)$$

$$= A_1^t A_1 + A_2^t A_2 + i(A_1^t A_2 - A_2^t A_1).$$

Symmetries of G

Using the properties of W , L and the trigonometric functions, the following symmetries are observed. Since $w(m,n)$ are real, $W(m,n, -\xi, -\zeta) = W^*(m,n, \xi, \zeta)$ and

$$G_{m,n}(-\xi, -\zeta) = G_{m,n}^*(\xi, \zeta)$$

we only need $G_{m,n}$ for $-K/2 \leq \xi < K/2$, $0 \leq \zeta < K/2$.

$G_{m,n}(\xi, \zeta) = G_{M-m,n}^*(\xi, \zeta)$, and we only need $G_{m,n}$ for $0 \leq \xi < K/2$, $0 \leq \zeta < K/2$.

$G_{m,n}(\zeta, \xi) = G_{M/4-m,n}(\xi, \zeta)$, and we only need $G_{m,n}$ for $0 \leq \xi < K/2$, $0 \leq \zeta < K/2$, $\zeta \leq \xi$.

The above symmetries define the group D_4 , the dihedral group of order 8. To incorporate the symmetries in the computations, we will use the following notation.

$$\sigma(\xi, \zeta) = (\zeta, -\xi); \quad S(m) = -M/4 + m, \\ G_{m,n}(\sigma(\xi, \zeta)) = G_{m,n}(\zeta, -\xi) = G_{S(m),n}^*(\xi, \zeta).$$

$$\rho(\xi, \zeta) = (\xi, -\zeta); \quad R(m) = M - m, \\ G_{m,n}(\rho(\xi, \zeta)) = G_{m,n}(\xi, -\zeta) = G_{R(m),n}^*(\xi, \zeta).$$

The group D_4 .

$$\sigma(\xi, \zeta) = (\zeta, -\xi), \rho(\xi, \zeta) = (\xi, -\zeta); \quad \sigma^4 = \rho^2 = 1; \quad \sigma\rho = \rho\sigma^3.$$

D_4 -orbital decomposition.

$$\begin{aligned} r_1 &= \{(\xi, \zeta) : -K/2 < \xi < 0, -K/2 < \zeta < \xi\}, & D_4(r_1) &= \{r_1, r_2, r_3, r_4, r_5, r_6, r_7, r_8\}. \\ l_1 &= \{(0, \zeta) : -K/2 < \zeta < 0\}, & D_4(l_1) &= \{l_1, l_2, l_3, l_4\}. \\ l_5 &= \{(\xi, 0) : -K/2 < \xi < 0\}, & D_4(l_5) &= \{l_5, l_6, l_7, l_8\}. \\ d_1 &= \{(\xi, \xi) : -K/2 < \xi < 0\}, & D_4(d_1) &= \{d_1, d_2, d_3, d_4\}, \\ p_1 &= \{(-K/2, -K/2)\}, & D_4(p_1) &= \{p_1\}. \\ p_2 &= \{0, -K/2\}, & D_4(p_2) &= \{p_2, p_4\}. \\ p_3 &= \{(0, 0)\}, & D_4(p_3) &= \{p_3\}. \end{aligned}$$

The orbital structure is given in the table below.

	I	σ	σ^2	σ^3	ρ	$\rho\sigma$	$\rho\sigma^2$	$\rho\sigma^3$
r_1	r_1	r_3	r_5	r_7	r_4	r_2	r_8	r_6
l_1	l_1	l_2	l_3	l_4	l_3	l_2	l_1	l_4
l_5	l_5	l_8	l_6	l_7	l_5	l_7	l_6	l_8
d_1	d_1	d_2	d_3	d_4	d_2	d_1	d_4	d_3
p_1	p_1	p_1	p_1	p_1	p_1	p_1	p_1	p_1
p_2	p_2	p_4	p_2	p_4	p_2	p_4	p_2	p_4
p_3	p_3	p_3	p_3	p_3	p_3	p_3	p_3	p_3

Denote the D_4 -asymmetric unit by Asy.

$$\text{Asy} = r_1 \cup l_1 \cup l_5 \cup d_1 \cup p_1 \cup p_2 \cup p_3.$$

Denote the associated row-permutations by S and R respectively,

$$S(m) = -M/4+m, \quad S^2(m) = -M/2+m, \quad S^3(m) = M/4+m, \quad S^4 = I.$$

$$R(m) = M-m, \quad R^2 = I.$$

Denoting the $M \times M$ permutation matrices again by S and R , we can express the symmetry conditions as follows.

$$\begin{aligned} G_{m,n}(\xi_i, \zeta) &= G_{m,n}(\xi_i, \zeta) \\ G_{m,n}(\sigma(\xi_i, \zeta)) &= G_{m,n}(\zeta, -\xi) = S G_{m,n}^*(\xi_i, \zeta), \\ G_{m,n}(\sigma^2(\xi_i, \zeta)) &= G_{m,n}(-\xi, -\zeta) = S^2 G_{m,n}(\xi_i, \zeta) = G_{m,n}^*(\xi_i, \zeta), \\ G_{m,n}(\sigma^3(\xi_i, \zeta)) &= G_{m,n}(-\zeta, \xi) = S^3 G_{m,n}^*(\xi_i, \zeta) = S G_{m,n}(\xi_i, \zeta), \\ G_{m,n}(\rho(\xi_i, \zeta)) &= G_{m,n}(\xi, -\zeta) = R G_{m,n}^*(\xi_i, \zeta), \\ G_{m,n}(\rho \sigma(\xi_i, \zeta)) &= G_{m,n}(\zeta, \xi) = RS G_{m,n}(\xi_i, \zeta), \\ G_{m,n}(\rho \sigma^2(\xi_i, \zeta)) &= G_{m,n}(-\xi_i, \zeta) = RS^2 G_{m,n}^*(\xi_i, \zeta) = R G_{m,n}(\xi_i, \zeta), \\ G_{m,n}(\rho \sigma^3(\xi_i, \zeta)) &= G_{m,n}(-\zeta, -\xi) = RS^3 G_{m,n}(\xi_i, \zeta) = RS G_{m,n}^*(\xi_i, \zeta). \end{aligned}$$

The computation

$$-K/2 \leq \xi_i, \zeta < K/2, \quad [G_{m,n}^+(\xi_i, \zeta)] r_m(\xi_i, \zeta)$$

is carried out by computing, for $(\xi_i, \zeta) \in \text{Asy}$,

$$\begin{aligned} [G_{m,n}^+(\xi_i, \zeta)] \quad r_m(\xi_i, \zeta), \quad S^3 r_m(-\zeta, \xi), \quad S^3 R r_m(\zeta, \xi), \quad R r_m(-\xi_i, \zeta) \\ [G_{m,n}^+(\xi_i, \zeta)]^* \quad S^3 r_m(\zeta, -\xi), \quad r_m(-\xi, -\zeta), \quad R r_m(\xi, -\zeta), \quad S^3 R r_m(-\zeta, -\xi). \end{aligned}$$

Let $r(\xi_i, \zeta)$ be indexed from 0 to $M-1$. Then the permutations $S^3 R$, R and S^3 are given in terms of the indices as follows;

$$S^3(m) = M/4+m, \quad S^3(0, 1, \dots, M-1) = (M/4, M/4+1, \dots, M-1, 0, 1, \dots, M/4-1), \\ \text{for } m = 0, m < M; m \rightarrow \text{mod}(m+M/4, M).$$

$$R(m) = M-m, \quad R(0, 1, \dots, M-1) = (0, M-1, M-2, \dots, 2, 1), \\ \text{for } m = 0, m < M, m \rightarrow \text{mod}(M-m, M).$$

$$S^3 R(m) = -M/4-m, \quad S^3 R(0, 1, \dots, M-1) = (3M/4, 3M/4-1, \dots, 2, 1, 0, M-1, M-2, \dots, \\ 3M/4+1), \text{ for } m=0, m < M; m \rightarrow \text{mod}(3M/4-m, M).$$

Incorporation of one of the symmetries has led to simplifying all the complex arithmetic in the matrix pseudo-inverse computation and related computations. This has reduced both memory requirement and complexity by over one half. One of the symmetry group elements relates rows of the system matrix. An additional symmetry, orthogonal has previously incorporated symmetries. These are obtained by factoring the matrix into two matrices, a diagonal matrix of phase factors and a dense matrix of coefficients similar to the original matrix. The dense matrix factor consists of columns, which are related by the reversal operator. Combining the row-wise and the column-wise symmetries, the dense matrices have been block-diagonalized into two-matrices of size $1/4$, reducing the storage requirements and complexity in the reconstruction.

4. Unitary Realization Of Complex Covariance Matrices:

Unitary realization of the covariance matrix in the Fourier domain has been implemented. As a result, all computations can be carried out in real arithmetic, yielding at least 4-fold speed-up in performance.

Organizing the three-dimensional hyperspectral data cube in the Fourier transform domain into a two-dimensional array by placing each frame into a column, covariance matrix C is obtained by

$$C = (FDf)^* (FDf),$$

where F is the spatial and f is the spectral Fourier transform of the data D . F is thus two-dimensional. Observe that

$$\begin{aligned} C &= f^* D' F^* F D f \\ &= (f^* D') (D f), \end{aligned}$$

Set $E = Df$,

$$E(x, u) = \sum_y D(x, y) \exp(-2 \pi i y u / N).$$

Since D is real, we have

$$E(x, N-u) = E^*(x, u).$$

Set $N = 4L$, $K = 2L + 1$ and define the $M \times K$ matrix B by

$$\begin{aligned} B(x, u) &= E(x, u), & \text{if } 0 \leq u \leq L, \\ B(x, u) &= E(x, u+2L-1), & \text{if } L+1 \leq u \leq 2L. \end{aligned}$$

B is the matrix of the lower half frequency information of E . Set

$$\begin{aligned} G &= B^* B, \\ G(m, n) &= \sum_k B^*(k, m) B(k, n). \end{aligned}$$

We will describe the symmetries of the $K \times K$ matrix G , which will be used to unitarily transform G into a symmetric, real matrix.

To describe the symmetries of G , first observe

$$B(x, K-u) = B^*(x, u), \quad 1 \leq u \leq K,$$

and $B(x, 0)$ is real valued.

By the definition of G , we have that G is transpose-conjugate invariant,

$$G^+ = G.$$

We also have that G is Hermitian symmetric,

$$G(K-m, K-n) = G^*(m, n), \quad 1 \leq m, n \leq K.$$

This follows since

$$\begin{aligned} G(K-m, K-n) &= \sum_k B^*(k, K-m) B(k, K-n) \\ &= \sum_k B(k, m) B^*(k, n) \\ &= G^*(m, n), \quad 1 \leq m, n < K, \\ G(K-m, 0) &= G^*(m, 0), \quad 1 \leq m < K, \\ G(0, K-n) &= G^*(0, n), \quad 1 \leq n < K, \end{aligned}$$

and $G(0, 0)$ and $G(m, m)$, $0 \leq n < K$, are real-valued. Decompose the matrix G by

$$\begin{array}{ccc} G(0, 0) & \mathbf{g}_0 & \mathbf{g}_1 \\ \mathbf{g}_2 & \mathbf{g}_4 & \mathbf{g}_5 \\ \mathbf{g}_3 & \mathbf{g}_6 & \mathbf{g}_7 \end{array}$$

where

$$\begin{aligned} \mathbf{g}_0 &= [G(0, 1) \quad G(0, 2) \quad \dots \quad G(0, L)], \\ \mathbf{g}_1 &= [G(0, L+1) \quad G(0, L+2) \quad \dots \quad G(0, 2L)], \end{aligned}$$

$$\begin{array}{ccc} \mathbf{g}_2 = G(1, 0) & & \mathbf{g}_3 = G(L+1, 0) \\ & G(2, 0) & G(L+2, 0) \\ & \vdots & \vdots \\ & \vdots & \vdots \\ & G(L, 0) & G(2L, 0) \end{array}$$

and the $L \times L$ submatrices are defined by

$$\begin{aligned}
\mathbf{g}_4(m,n) &= G(l+m, l+n), \\
\mathbf{g}_5(m,n) &= G(l+m, l+L+n), \\
\mathbf{g}_6(m,n) &= G(l+L+m, l+n), \\
\mathbf{g}_7(m,n) &= G(l+L+m, l+L+n), \quad 0 \leq m, n < L.
\end{aligned}$$

To describe the relationships between the submatrices, define the $L \times L$ reversal matrix R by

$$R = \begin{pmatrix} 0 & 0 & \dots & 0 & 1 \\ 0 & & & 1 & 0 \\ & & & & \\ & & & & \\ 1 & 0 & \dots & 0 & 0 \end{pmatrix}$$

Multiplication on the right by R reverses the rows and multiplication on the right reverses the columns.

$$\begin{aligned}
\mathbf{g}_l &= [G(0, L+1) \quad G(0, L+2) \quad \dots \quad G(0, 2L)] \\
&= [G^*(0, K-L-1) \quad G^*(0, K-L-2) \quad \dots \quad G^*(0, K-2L)] \\
&= \mathbf{g}_0^* R.
\end{aligned}$$

The transpose-conjugate invariance of G implies that

$$\mathbf{g}_4^+ = \mathbf{g}_4, \quad \mathbf{g}_0^+ = \mathbf{g}_2.$$

Application of the above two arguments shows that

$$\begin{aligned}
\mathbf{g}_3 &= R \mathbf{g}_0^t. \\
\mathbf{g}_6(m,n) &= G(l+L+m, l+n) \\
&= G^*(K-l-L-m, K-l-n) \\
&= G^*(l+L-l-m, l+L-l-n) \\
&= R \mathbf{g}_5^*(m,n) R.
\end{aligned}$$

$$\begin{aligned}
\mathbf{g}_7(m,n) &= G(l+L+m, l+L+n) \\
&= G^*(K-l-L-m, K-l-L-n) \\
&= G^*(l+L-l-m, l+L-l-n) \\
&= R \mathbf{g}_4^*(m,n) R.
\end{aligned}$$

$$\begin{aligned}
\mathbf{g}_5(m,n) &= G(l+m, l+L+n) \\
&= G^*(l+L+n, l+m) \\
&= G^*(K-l-L-n, K-l-m) \\
&= G^*(l+L-l-n, l+L-l-m) \\
&= R \mathbf{g}_5^t(m,n) R.
\end{aligned}$$

Thus, we have that the matrix G is of the following form.

$$\begin{array}{lll}
G(0,0) & g_0 & g_0^* R \\
g_0^+ & g_4 & g_5 \\
R g_0^+ & R g_5^* R & R g_5^* R
\end{array}$$

5. Singular Value Decomposition Of The Data Matrix:

Singular value decomposition (SVD) is at the core of principal component analysis for image reconstruction and interpretation. A literature search on coarse grained parallel algorithms has led to the conclusion that thus far, there does not exist numerically stable, tested algorithms [1]. A further literature search was carried out for efficient SVD algorithms for special cases: The initial reconstructed image is three-dimensional, consisting of two space dimensions and one spectral dimension. The principal component analysis is based on selection of the spectral bands of significant information. Thus the image data is treated as a two-dimensional array with a row dimension determined by the spatial index and the column dimension determined by the spectral index. This arrangement of the data results in an array with very high row/column ratio. T. Chan reports very favorable performance of an implementation that exploits the high row/column ratio [7]. Briefly, the algorithm is an hybrid method of QR factorization and SVD: Given a two-dimensional array A , QR factorization yields the decomposition $A = Q R$, where Q is an orthogonal matrix, i.e., $Q^T Q = I$, with Q^T the transpose of Q and I the identity matrix, and R is an upper triangular matrix. If A is an $m \times n$ array, then the matrix R is of rank at most n . In fact, the entries of R are nonzero only for the first n rows. Denote the $n \times n$ nonzero upper triangular submatrix of R by R' . The SVD of R' results in the decomposition $R' = U W V^T$, where U and V are $n \times n$ orthogonal matrices and W is an $n \times n$ diagonal matrix. It is easy to prove that the SVD of R is then given by $R = (QU) W V^T$. The advantage in this hybrid algorithm is two fold: First, the QR factorization is of less complexity than SVD of an equal size array; SVD is computed on an array of size $n \times n$. Thus in case where $m \gg n$, the complexity should reduce substantially. This idea will be investigated through implementation. The first step in the proposed algorithm is the sequence of left Householder transformations to reduce the array to an upper triangular matrix. This requires accessing data at stride of the number of columns of the data array. This can be implemented as a single sweep of data transfers as matrix transpose. Left transformation by Householder or Givens is also required in the current implementation of SVD. The "transposed" algorithm was implemented: Up to pre- and post processing of data permutation, the transposed algorithm performs significantly different depending on the size and shape of the data matrix. Bench mark cases were run for various sizes and shapes of arrays with performance comparisons ranging from 0% to 60% improvements. As a computational tool in the principal component analysis, this has led to many fold increase in performance.

7. Eigen Decomposition Algorithm And Implementation:

The modification and implementation of an eigen decomposition algorithm given in *Numerical Recipes in C*, by W. Press, et al. has been implemented. The algorithm is based on successive Housholder reduction. Modification of the data structure in terms of sequential data accessing has been incorporated. This routine is used as a preprocessing stage to singular value decomposition of highly rectangular data array. The eigen decomposition of a square array A is

$$A = E w E^T,$$

where the square array E of eigen vectors is unitary, i.e., $E^T E = I$, and the matrix w of eigen values is diagonal. On the other hand, the singular value decomposition of an arbitrary matrix B of size $M \times N$, $M \geq N$ is

$$B = U \omega V^T,$$

where U is a unitary matrix of size that of B , V is a unitary matrix of square size $N \times N$, and ω is an $N \times N$ diagonal matrix of singular values. Let $U \omega V^T$ be the singular value decomposition of B . Then

$$B^T B = (U \omega V^T)^T U \omega V^T = V \omega^T U^T U \omega V^T = V \omega^2 V^T,$$

since $U^T U = I$ and ω is transpose invariant. The uniqueness of the singular value decomposition now yields, the eigen decomposition of the covariance matrix $B^T B$. Reversing the argument, we have that the two of the factors in the form of singular value decomposition is obtained from the eigen decomposition, namely the matrices V^T and $w = \sqrt{\omega}$. For a highly rectangular matrix A of size $M \times N$, $M \gg N$, the complexity of eigen decomposition of the covariance matrix is significantly better than the singular value decomposition. The matrix U can be constructed by

$$U = A V w^{-1/2}.$$

This method is not commonly used due to lack of accuracy. However, in the case of data analysis by significant components, only a few of the columns of U is sought: The columns of U associated with the few largest singular values. Thus accuracy of these columns is satisfactory, and the complexity issues overweigh the accuracy trade-off.

References

1. J. Mooney, V. Vickers, A. Brodzik and M. An, "High-throughput hyperspectral infrared camera," *J. Opt. Soc. Am. A*, **14**(11), 1997.
2. A. Brodzik, J. Mooney and M. An, "Image restoration by convex projections: Application to image spectrometry," Proceedings of SPIE96, Denver.
3. J. Mooney, A. Brodzik and M. An, "Principal Component Analysis in Limited-Angle Chomotomography," presented at SPIE97 in San Diego and published in the preceedings.
4. R. Tolimieri, M. An and C. Lu, *Algorithms for diacrete Fourier transform and convolutions*, 2Ed, Springer-Verlag, 1997, NY.
5. R. Tolimieri, M. An and C. Lu, *Mathematics of multidimensional Fourier transform algorithms*, 2Ed, Springer-Verlag, 1997, NY.
6. *Numeral Recipes in C*, by W.H. Press, S.A. Teukolsy, W.T. Vetterling and B.P. Flannery, Cambridge University Press, 1995.
7. "An Improved Algorithm for Computing the Singular Value Decomposition," by T. Chan, *ACM Transactions on Mathematical Software*, **8**(1), 1982.

TECHNICAL ACTIVITY:

In the beginning of this program, wafers were being processed using the standard PtSi process. The first step was to modify this process so that the substrate contact areas would have a p+ impurity concentration before aluminum metallization. In the new process the field oxide was removed and a 200 Å oxide was grown in the substrate contact areas. Next the contact areas were implanted with a high dose (3×10^{15}), low energy (30 KeV) BF_2 implant. The wafers were then annealed to activate the implant. All the thermal cycles were adjusted to preserve the guard ring profile.

This modification to the process made it much more flexible. Wafers could now be processed so others outside the laboratory could use them for various applications. For example, wafers in batch 9 were processed for Mr. Richard Strong. He wanted to deposit a Si-Ge alloy selectively in the active areas and thus reduce the number of processing steps. In order to be able to deposit material in the active areas selectively, there must be some oxide covering the areas where no deposition is desired while the active areas are etched oxide free. This condition required having at least 500 Å of SiO_2 over areas where the deposition was unwanted. This requirement was met by modifying the oxide growth step prior to the BF_2 contact implant. The dose and energy of the various implants as well as the thermal cycles were adjusted to keep the impurity profiles the same. Wafers were also processed for Mr. Davis Lange. He needed to deposit various materials to form Schottky diodes in the active areas. These diodes were made by blanket deposition and thus subsequent to the diode formation, the unwanted material had to be removed by sputtering. The latter was not satisfactory because the photoresist was adversely affected during the sputtering process and was very difficult to remove.

After the process development was completed, a need for a new mask set was realized so the process could be more flexible for different applications. The complete mask set had nine layers and could be used to process 2", 3", and 4" wafers. Also, new variations of the standard devices could be processed using these masks. To study the effect of various guard ring profiles on the device properties, many smaller sizes (active areas ranging from $10 \mu\text{m} \times 10 \mu\text{m}$ to $200 \mu\text{m} \times 200 \mu\text{m}$), in addition to the standard $500 \mu\text{m} \times 500 \mu\text{m}$ devices, were also incorporated. The idea was to be able to look at the effective active areas of devices with shallower guard rings. The effect was expected to be the most pronounced in smaller (e.g. $10 \mu\text{m} \times 10 \mu\text{m}$) devices but the signal output from a single small device was not expected to be big enough for accurate measurements. To enhance the signal from smaller devices, a number of them, each having their own guard ring, were strung together to present a larger effective active area. This mask set also incorporated devices so that the guard ring and the active areas could be independently biased. There were devices of various sizes with and without guard rings and also under and oversized active area layers to be used when the Schottky material had to extend beyond the active area.

A number of wafers were processed using this new set of mask for different applications. Batch 13 was processed using the standard PtSi process to qualify the mask set while the last of the remaining batches were completed using the old masks. Batch 11 was processed with the old CLD masks using 30-40 $\Omega\text{-cm}$, 2" wafers. The purpose of this batch was to fabricate devices on high resistance substrates while modifying the active area profile by implantation. The results of this experiment were inconclusive as the devices tended to breakdown at low voltages.

Devices were fabricated using the new mask sets, which were to be used by Mr. Jimenez in collaborative experiments with JPL. Devices were also fabricated to be used in collaborative experiments with NRL. The new mask set was also used to fabricate devices with guard ring depths of 1 μm , 0.75 μm , 0.5 μm , and 0.25 μm . The guard ring implant energies, doses and the thermal cycles were modified to obtain these profiles. All of these devices had good characteristics.

At this time the emphasis on the type of devices to be studied had changed. It was decided that an uncooled temperature sensor should be fabricated and looked at electrically. The devices would have to be thermally isolated from the substrate and the heat loss in the leads, which were not completely thermally isolated from the bulk had to be minimized. These devices were to be fabricated in the Integrated Circuits Laboratory (ICL) at the Massachusetts Institute of Technology (MIT). Thermal isolation of the devices from the substrate by isotropic etching of silicon under the devices was also to be carried out at MIT. A new set of masks were designed and fabricated to be used in the ICL, which would use the 10X stepper as the photolithography tool.

Wafers were fabricated at MIT and some etching experiments were carried out. Preliminary experiments were promising. At the same time it was decided to keep fabricating CoSi_2 diodes in house. A CoSi_2 Schottky diode was to be used as the sensor element in the thermal detector. These diodes were fabricated on SOI wafers having a thin ($\approx 2300 \text{ \AA}$) top silicon layer. CoSi_2 diodes were formed by sputter deposition of cobalt and in situ annealing at 400° to form CoSi . The second anneal at 740°C to form CoSi_2 was done in a furnace (rather than RTA, the results of which were not very repeatable). Unreacted cobalt was removed by dipping the wafers in piranha for 1 minute. Measurements on these devices resulted in good diode characteristics but abnormally low values of A^* . To improve the values of A^* , the top silicon layer of the SOI wafers was implanted to increase the p impurity concentration. The peak of the implants was kept away from the top silicon surface to keep the later as defect free as possible and also to not change the impurity concentration near the surface where the devices were to be formed. These experiments were very successful in improving the value of A^* . These experiments were also repeated in wafers where the top silicon layer was thicker (5 μm) and were satisfactory ($A^* \approx 32.1$ to 39.7 , barrier height = 0.38eV). These experiments were also repeated with PdSi as the thermal detector.

The next step was to optimize the thickness of the top silicon layer for the device application in the Thermoionic Thermal Detector. SOI wafers were sent away for depositing epi silicon so that the top silicon layers were of 0.5 μm , 0.75 μm , 1 μm , and 1.25 μm thickness respectively. Devices using both CoSi_2 and PdSi were successfully formed on wafers having 0.5 μm and 0.75 μm top layers. These wafers were implanted with boron (Dose = 4×10^{12} , $E = 100 \text{ KeV}$) through a 500 \AA thermal oxide before silicide formation.